A Multiscale Numerical Study of Hurricane Andrew (1992). Part I: Explicit Simulation and Verification

YUBAO LIU

Department of Atmospheric and Oceanic Sciences, McGill University, Montreal, Quebec, Canada

DA-LIN ZHANG

Department of Meteorology, University of Maryland at College Park, College Park, Maryland

M. K. YAU

Department of Atmospheric and Oceanic Sciences, McGill University, Montreal, Quebec, Canada

(Manuscript received 16 July 1996, in final form 2 April 1997)

ABSTRACT

In this study, the inner-core structures of Hurricane Andrew (1992) are explicitly simulated using an improved version of the Penn State–NCAR nonhydrostatic, two-way interactive, movable, triply nested grid mesoscale model (MM5). A modified Betts–Miller cumulus parameterization scheme and an explicit microphysics scheme were used simultaneously to simulate the evolution of the larger-scale flows over the coarser-mesh domains. The intense storm itself is explicitly resolved over the finest-mesh domain using a grid size of 6 km and an explicit microphysics package containing prognostic equations for cloud water, ice, rainwater, snow, and graupel. The model is initialized with the National Centers for Environmental Prediction analysis enhanced by a modified moisture field. A model-generated tropical-storm-like vortex was also incorporated. A 72-h integration was made, which covers the stages from the storm's initial deepening to a near–category 5 hurricane intensity and the landfall over Florida.

As verified against various observations and the best analysis, the model captures reasonably well the evolution and inner-core structures of the storm. In particular, the model reproduces the track, the explosive deepening rate (>1.5 hPa h^{-1}), the minimum surface pressure of 919 hPa preceding landfall, the strong surface wind (>65 m s^{-1}) near the shoreline, as well as the ring of maximum winds, the eye, the eyewall, the spiral rainbands, and other cloud features. Of particular significance is that many simulated kinematics, thermodynamics, and precipitation structures in the core regions compare favorably to previous observations of hurricanes.

The results suggest that it may be possible to predict reasonably the track, intensity, and inner-core structures of hurricanes from the tropical synoptic conditions if high grid resolution, realistic model physics, and proper initial vortices (depth, size, and intensity) in relation to their larger-scale conditions (e.g., SST, moisture content, and vertical shear in the lower troposphere) are incorporated.

1. Introduction

The hurricane is a violent atmospheric vortex characterized by strong multiscale interactions. Its horizontal extent is typically several hundred to a thousand kilometers, but the energy responsible for the whole system is mainly released in convective cells only a few kilometers across. Previous studies have shown that the tropical synoptic conditions and the sea surface temperature (SST) tend to control the general development of a hurricane (Gray 1979; Emanuel 1988; DeMaria and Pickle 1988). However, its track and intensity can be affected by its internal dynamics and thermodynamics, the formation and distribution of clouds and precipitation, and the interaction between the hurricane and its larger-scale environment (Holland and Merrill 1984; Molinari and Vollar 1995; Ross and Kurihara 1995; Willoughby and Black 1996). The interaction of different scales of phenomena poses special difficulties in modeling hurricanes because it requires huge computer resources and accurate representation of physical processes over a wide range of scales. As a result, various approximations have to be made, and only certain aspects of hurricane-genesis processes can be examined.

Numerical simulation of hurricanes originated in the early 1960s with axisymmetric models, in which the flow variations in the azimuthal direction are ignored (e.g., Kasahara 1961; Ooyama 1969; Sundqvist 1970).

Corresponding author address: Dr. Da-Lin Zhang, Department of Meteorology, University of Maryland at College Park, 3433 Computer and Space Sciences Bldg., College Park, MD 20742-2425.
E-mail: dalin@atmos.umd.edu

Since the 1970s, more sophisticated models have been developed. They can be classified into two general groups. Models in the first group, using a grid resolution of 20–100 km, were used to examine the system-scale properties of a hurricane vortex. Latent heating is parameterized in various ways, ranging from the specification of heating profiles to the simple removal of supersaturation, the popular Kuo (1965, 1974) cumulus scheme and the simultaneous treatment of subgrid- and grid-scale precipitation (e.g., Anthes 1972; Krishnamurti et al. 1995). The well-known Geophysical Fluid Dynamics Laboratory (GFDL) hurricane model uses the Kurihara (1973) moist convective adjustment scheme with grid resolutions ranging from 5 km to over 100 km (Tuleya et al. 1984; Kurihara 1985; Kurihara et al. 1995). Obviously, these models display a large sensitivity to the way the convective heating is parameterized and how the grid-scale condensation is treated.

Models in the second group are cloud models with high horizontal resolutions (<20 km), which were designed to explicitly simulate deep convection, the eyewall, and the eye at the central core of hurricanes. The axisymmetric model of Yamasaki (1977) has a domain with a radius of 60 km and a grid spacing of 400 m near the central axis. It generated an intense hurricane with a central pressure 100 hPa lower than its environment. The simulated eye is extremely small, with a diameter of 3–4 km. He found that the complicated unbalanced mass and wind fields associated with differential heating generate inflow during the early stages of the hurricane development. Rosenthal (1978) reported an interesting (hydrostatic) simulation using a simple explicit moisture scheme but with a grid size of 20 km. His model hurricane reached a depth comparable to that of Yamasaki's, in spite of the much larger grid size. In the above two models, hurricanes started from squall-line-like convection. Then, surface winds intensified and convective bands contracted in scale to form the eyewall. Using a nonhydrostatic model with a sophisticated cloud microphysics scheme, Willoughby et al. (1984a) and Lord et al. (1984) simulated many more realistic features of mature hurricanes, including the outward sloping of updrafts in the eyewall, the concentric convective rings, and the stratiform rain and mesoscale downdrafts outside the eye. Rotunno and Emanuel (1987) constructed a similar model to study the effect of air–sea interaction on the development of the hurricane.

Most of the models mentioned above are axisymmetric with calm environmental winds to begin with. They are clearly unsuitable for investigating the asymmetric nature, the storm-environment interaction, the genesis and landfall of hurricanes, and for testing different environmental conditions. A fully three-dimensional (3D) model is therefore required to study the more realistic development of hurricanes. Anthes et al. (1972) were the first to simulate the structures of asymmetric outflows and spiral rainbands using a 3D hydrostatic model with a grid length of 30 km. Jones (1977) constructed a sophisticated triply nested-grid system to model simultaneously the dynamics of a hurricane and the interaction with its environment. The simulated asymmetric ring (radius) of maximum winds (RMW) and the spiral convergent flow are similar to those observed in mature hurricanes. Kurihara and Bender (1982) simulated the detailed eye structure of intense hurricanes using a quadruply nested grid, hydrostatic model with the finest mesh size of 5 km. Tripoli (1992) carried out a nonhydrostatic 3D simulation and obtained more realistic structures of hurricane rainbands.

Numerical models have also been employed to predict hurricane-related features (see the reviews by Elsberry 1979 and Anthes 1982). The earlier operational predictions were only limited to hurricane tracks. More recently, trial runs for predicting the intensity and structures of hurricanes are conducted with high-resolution (20–50 km) models and more sophisticated model physics (Kurihara et al. 1993; Krishnamurti et al. 1995). Through case studies, Krishnamurti et al. (1989, 1995) demonstrated that their high-resolution global model can forecast the deepening process and the signature of spiral-type rainbands a few days in advance. Bender et al. (1993) showed that the GFDL hurricane model has some skill in predicting the deepening and the development of strong winds, but it tends to overpredict weak hurricanes and underpredict strong ones.

On the other hand, observations into numerous intense hurricanes (e.g., Inez of 1966, Anita of 1977, Frederic of 1979, David of 1979, Allen of 1980, Alicia of 1983, Norbert of 1984, Gloria of 1985, Emily of 1987, Hugo of 1989, Claudette of 1991, Andrew of 1992, etc.) using instrumented aircraft with onboard radar have been made in the past years. These observations reveal many interesting phenomena and structures of mature hurricanes, particularly in terms of the dynamics, thermodynamics, and the microphysics of the eye, the eyewall, the stratiform rain regions, and the outlying spiral rainbands (e.g., Gray and Shea 1973; Hawkins and Imbembo 1976; Willoughby et al. 1982; Jorgensen 1984a; Black and Hallett 1986; Willoughby 1990; Marks and Houze 1987; Marks et al. 1992; Houze et al. 1992; Roux and Viltard 1995, etc.). Based on the observations, Willoughby et al. (1982) proposed a mechanism for the formation of contracted concentric eyewalls. Jorgensen (1984b) presented a conceptual model for the inner core of Hurricane Allen (1980). Marks et al. (1992) composited the 3D wind field to show the structure of two internal gyres in the core region of Hurricane Norbert (1984). Houze et al. (1992) found the development of significant amount of graupel in the updrafts of the eyewall of the same storm. The transport of small ice particles by the airflow in the core region appears to determine profoundly the out-of-core stratiform precipitation. The complexities revealed by the observations indicate a need for the use of high resolutions and sophisticated microphysics parameterizations to model properly the structures of these tropical storms. The measurements also provide the ground truth for verifying the performance of numerical models.

From the above review, it is clear that the previous hurricane models are limited in one or more of the following aspects: balance approximation, axisymmetric assumption, low resolution, hydrostatic dynamics, crude physical parameterizations, idealized initial conditions, and inability to treat multiscale interactions. Because of these limitations, we have not seen a single real-data simulation of a hurricane in the literature where multiscale interactions and its core structures are explicitly resolved. Thus, it is the intention of this study to fill this gap by using the state-of-the-art Pennsylvania State University–National Center for Atmospheric Research (PSU–NCAR) mesoscale model (i.e., MM5) to simulate explicitly the development of Hurricane Andrew (1992). In this study, the model is initialized with the National Centers for Environmental Prediction (NCEP) analysis and then verified against various observations, including Omega dropwindsondes (ODWs), satellite, ground-based radar, dense surface observations at landfall and the best track analysis. We believe that *given the SST and the low-level moisture and flow fields, successful prediction of hurricanes from the tropical synoptic conditions can be achieved if high grid resolution, realistic model physics, and proper initial vortices (depth, size, and intensity) are incorporated.* The objectives of the present paper are to (i) document the methodology, the necessary model physics and its associated improvements that are used to simulate explicitly the inner-core structures of Hurricane Andrew; (ii) demonstrate the predictability of some hurricane-scale features from the synoptic-scale initial conditions through verification of the model simulation against available observations; and (iii) present some detailed 3D structures in the core region of the storm in order to establish credibility for further diagnostic analyses and sensitivity simulations to be presented in subsequent parts of this series of papers.

This paper is organized as follows. The next section provides a brief overview of Hurricane Andrew (1992). Section 3 describes the basic features and improvements of the PSU–NCAR model (MM5) as well as the model design. Initialization of the movable, triply nested meshes and construction of an initial vortex will also be discussed. Section 4 presents the structures and evolution of Hurricane Andrew and provides verification of the model simulation against all available observations. Section 5 shows the simulated central-core structures of the storm, as compared to the observations of other hurricanes. A summary and conclusions are given in the final section.

2. Overview of Hurricane Andrew

Hurricane Andrew can be labeled the most expensive natural disaster in the history of the United States. It cost a total of \$25 billion in damages (see Wakimoto and Black 1994; NOAA 1992). The storm originated from a tropical disturbance near the west coast of Africa on 14 August. On 16 August, it was classified as a tropical depression (i.e., with $V_{\max} < 18$ m s^{-1} at the surface) when it traveled to about 3000 km to the east of the Lesser Antilles Islands. The storm gradually strengthened during its northwestward movement. Deep convection began to organize into a narrow, spiral cloud band on 17 August. The system was subsequently upgraded to Tropical Storm Andrew, when the estimated surface winds exceeds 18 m s^{-1}. During the following two days, however, the storm appeared to encounter an unfavorable environment, which interrupted its otherwise continued deepening. Specifically, a large-scale high pressure area was lying to its north and a strong upper-level low was located to its west-northwest. The low extended southward into the lower troposphere and it, together with the northern high, generated strong southwesterly vertical shear in Andrew's environment. This condition damped substantially the intensity of the storm; its central pressure increased 15 hPa to an incredibly high value of 1015 hPa at 1800 UTC 20 August.

On 21 August 1992, the upper-level trough began to split. The northern low changed into a trough and it retreated farther northward, leading to decreased vertical shear in Andrew's environment. The remainder of the low drifted southward, generating an upper-level outflow over Andrew. Meanwhile, a strong and deep subtropical high formed off the southeast coast of the United States, with its ridge axis lying just to the north of the storm. This generated an easterly steering flow for the storm. With these dramatic changes in its environmental conditions, Andrew turned westward and began its explosive development. It deepened to hurricane strength (i.e., surface $V_{\max} > 33$ m s^{-1}) on 22 August. From 0000 UTC 21 to 1800 UTC 23 August, its central pressure fell 92 hPa, that is, from 1014 to 922 hPa. The deepening rate of 2.2 hPa h^{-1} matches the rapid deepening hurricane defined by Holliday and Thompson (1979). According to the Saffir–Simpson hurricane scale (Simpson 1974), Andrew only took 36 h to develop from a tropical storm to a near–category 5 hurricane.

After reaching its maximum intensity, Hurricane Andrew experienced a temporary weakening, probably through a process of concentric eyewall contraction (Willoughby and Black 1996). It reintensified to 922 hPa with a maximum surface wind of 67 m s^{-1} just before landfall when it moved over the warm straits of Florida (see Fig. 1a). Then, Andrew weakened by one category in the process of crossing Florida in a period of 4 h (i.e., from 0830 UTC to 1230 UTC 24 August) due to the presence of stronger surface friction and smaller surface heat fluxes over land. The storm left Florida with a central pressure of 951 hPa and strengthened again as it moved over the warm water of the Gulf of Mexico. On 25 August, the hurricane reduced its forward movement and recurved in a northwest direc-

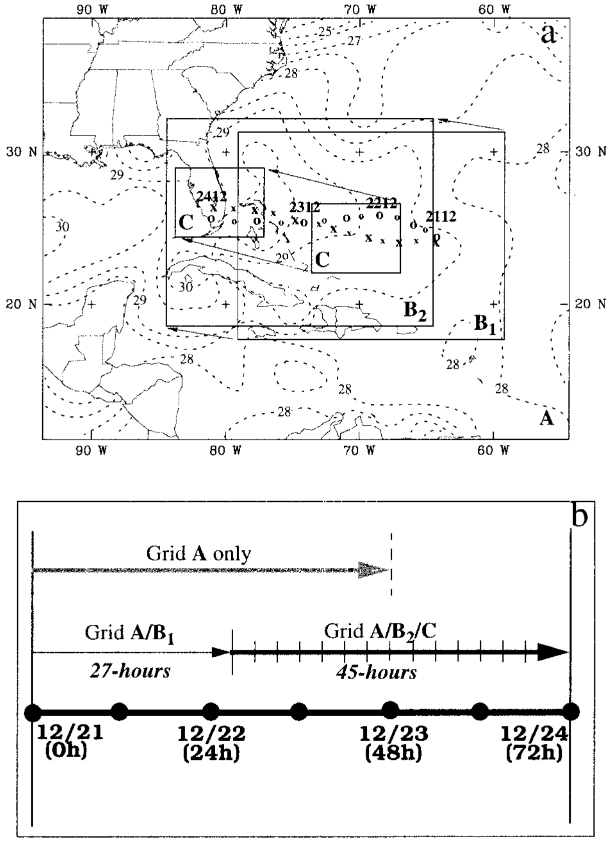

FIG. 1. Design of (a) model domains and (b) model integration (see Table 1 for more detailed information). Tracks of Hurricane Andrew from the 6-h best track analysis ("○") by Mayfield et al. (1994) and the model output ("×") are given in (a), together with the SST field (dashed) at intervals of 0.5°C. Larger fonts denote the positions of Hurricane Andrew every 12 h, with the corresponding date and time given.

TABLE 1. The model design.

Domain	Mesh A	Mesh B	Mesh C
Dimensions (x, y)	82 × 64	124 × 94	124 × 94
Area coverage (km^2)	4374 × 3402	2214 × 1674	738 × 558
Grid size (km)	54	18	6
Time step (s)	120	40	13.33
Integration hours	0–72	B_1: 1–27; B_2: 27–72	27–72

tion toward Louisiana under the influence of a traveling large-scale trough in the westerlies. Andrew struck south-central Louisiana on 26 August. It weakened rapidly after landfall and was reduced to tropical depression intensity in 12 h. The system completed its life cycle on 28 August after merging with a frontal system over the mid-Atlantic states. For more detailed observational analyses of the storm, the reader is referred to Mayfield et al. (1994), Rappaport (1994), and Willoughby and Black (1996).

Our model integration is initialized at 1200 UTC 21 August when Andrew just began to intensify in a newly formed favorable environment. The run is terminated at 1200 UTC 24 August when it was about to move out of Florida. This 72-h integration covers the most important period of the life cycle of Hurricane Andrew, including its rapid deepening stage, the mature stage, the maximum intensity stage near Bahamas, and particularly, its landfall stage over Florida. The simulation of Andrew's landfall over Florida also allows us to verify the model using detailed observations over land and nearshore water surfaces.

3. Model description and initial conditions

An improved version of the PSU–NCAR nonhydrostatic, movable, triply nested grid, 3D mesoscale model [i.e., MM5; see Dudhia (1993) and Grell et al. (1995)] is used for the present study. The nonhydrostatic version employs the same terrain-following σ coordinate as in the hydrostatic version of the model (i.e., MM4; see Anthes et al. (1987)], but the pressures at the σ levels are determined from a reference state that is estimated using the hydrostatic equation from a given sea level pressure and temperature with a standard lapse rate. There are 24 uneven σ levels or 23 σ layers (for all grid meshes) with higher resolution in the planetary boundary layer (PBL). The σ levels are placed at values of 1.0, 0.99, 0.98, 0.96, 0.93, 0.89, 0.82, 0.75, 0.68, 0.61, 0.54, 0.47, 0.41, 0.35, 0.30, 0.25, 0.21, 0.17, 0.14, 0.11, 0.08, 0.05, 0.02, and 0. The nonhydrostatic equations are solved by integrating the acoustic terms with a smaller time step, while using a longer time step for slow-mode terms (Klemp and Wilhelmson 1978).

A two-way interactive, movable, triply nested grid technique, based on monotonous interpolation (Smolarkiewicz and Grell 1992), is employed to achieve the multiscale simulations. Figure 1a shows the three model domains used, and Table 1 describes the domain design. The outermost mesh A domain is fixed and it is designed to simulate the synoptic-scale environment in which the system evolves. The size of the domain is chosen sufficiently large to minimize the influence of the lateral boundary conditions on the evolution of Andrew. The intermediate mesh B domain is used to simulate the hurricane-scale flows. The B_1 and B_2 domains cover, respectively, the initial slow and the subsequent rapid intensification stages of the storm. The domain is moved only once, that is, from B_1 to B_2, at 27 h into the integration. The finest mesh C domain with a grid size of 6 km is designed to resolve explicitly the central core and spiral rainbands of the storm. Coarser meshes provide finer meshes with time-dependent lateral boundary conditions while the finer-mesh solutions are fed back to coarser meshes every time step, thereby achieving the two-way interaction of the meshes. The outermost lateral boundary conditions (i.e., for mesh A) are specified by linearly interpolating the 12-h observational analysis according to Perkey and Kreitzberg (1976). To reduce the computational cost, mesh C is activated at 27 h into the integration when more organized grid-scale condensation over the mesh B domain begins to develop. Mesh C is moved within the mesh B domain once every 3 h to track the movement of the hurricane (see Fig. 1).

The model water cycles include the simultaneous use of the Betts–Miller (1986) deep and shallow convective parameterization and the Tao–Simpson (1993) cloud microphysics scheme for the 54- and 18-km grid meshes, but only the latter is used for the 6-km grid mesh. Zhang et al. (1988) and Molinari and Dudek (1992) demonstrated that for a grid size larger than 10 km, the coupling of parameterized convection with explicit moisture schemes tends to have the greatest potential success in reproducing the development of different mesoscale convective systems (MCSs). However, for a grid size of 6 km, convective parameterization could be bypassed. Note that to properly simulate the organized convection, the Betts–Miller scheme has been modified to relate the triggering of deep convection to grid-scale vertical motion, in a manner similar to that in Kain and Fritsch (1992). Note also that the Betts–Miller parameterization for shallow convection is applied over mesh C to treat reasonably shallow convective clouds at the outer edge of the hurricane. The Tao–Simpson (1993) microphysics scheme, which is modified from Lin et al. (1983), contains prognostic equations for cloud water (ice), rainwater (snow), and graupel, and it allows for the generation of supercooled water, which is not available in the scheme used by Dudhia (1989) and Zhang (1989). In the present case, graupel is defined as ice particles with a density of 0.4 g cm^{-3} and a diameter greater than 5 mm. The definition is consistent with microphysics observations in different hurricanes (see Black and Hallett 1986; Marks et al. 1992).

Other model physics include a modified version of the Blackadar (1979) PBL parameterization (Zhang and Anthes 1982) and a cloud–radiation interaction scheme (Dudhia 1989; Grell et al. 1995). The SST is held constant during the integration and friction at the sea surface is calculated with a roughness length that is dependent on surface wind speeds. The land surface temperature is predicted using surface energy budget equations, in which the effects of short- and longwave radiation and cloud radiation are included. For a more detailed description of MM5, the reader is referred to Dudhia (1993) and Grell et al. (1995).

The model is initialized at 1200 UTC 21 August 1992 with the NCEP 2° (latitude–longitude) resolution analysis, which is then enhanced by rawinsondes, surface observations, and the navy's SST field. Note the increasing SST along the track of the storm, with maximum values exceeding 29.5°C over the straits of Florida (Fig. 1a). The increasing SST was well correlated with the continued rapid deepening of the storm as it moved westward. An inspection of the NCEP analysis reveals the presence of a cyclonic circulation corresponding to the prehurricane disturbance in the tropical easterlies. However, the analysis fails to capture the right scale and intensity of the tropical storm, as compared to the analyses of Mayfield et al. (1994), Rappaport (1994), and Willoughby and Black (1996), because there are few upper-air observations over the vast tropical oceans and because the 2° analysis grid resolution is too coarse to resolve it. Therefore, it is necessary to incorporate into the initial conditions a tropical-storm-like vortex with a realistic size, depth, and intensity. Kurihara et al. (1993, 1995) have shown that this procedure is instrumental in improving the first 24- to 48-h forecast of the tracks and strength of hurricanes. For this reason, we run mesh A first with full physics for 48 h (see Fig. 1b), at which time the model-generated vortex reached its minimum central pressure similar to the best analysis at the model initial-time. Then, the vortex is extracted in 3D and merged into the initial conditions with the location of the center consistent with that in the best track analysis. This methodology does not produce any notable ‘‘shocks’’ once the model is integrated, since all the meteorological fields in the tropical easterlies are relatively uniform and since the storm under study tracks nearly westward during the 48-h period (i.e., little changes in the Coriolis parameter). Furthermore, the vertical circulation (vorticity) structures so generated tend to be more compatible with the model dynamics and with the initial larger-scale conditions than the case of an arbitrarily bogused vortex.

In addition to the structure and intensity of the prehurricane, we found from initial experimentation with a resolution of 54 km that the vortex environment in the NCEP analysis is always too dry, particularly in the lower troposphere, as compared to the ODW observations that were taken during Andrew's development stage. Therefore, the initial relative humidity field is modified in accordance with the ODW observations by setting its value over the ocean to no less than 85% for the layers below 800 hPa, and for the layers from the surface to 300 hPa within the vortex (with a radius of 150 km). This modification appears to facilitate the triggering of deep convection and grid-scale condensation associated with the storm during the first 24-h integration, as verified against satellite observations.

For the finer-mesh domains (i.e., B and C), the initial conditions are always interpolated from the coarser-mesh data. This is also true for data in the leading portion of the finer-mesh domains when they are undergoing translation. Table 1 and Fig. 1 can be referred to for a more detailed description of the initialization and integration procedures.

4. Model verification

In this section, we verify the 72-h simulation, mainly from mesh C with a grid size of 6 km, against various observations (e.g., ODWs, surface analyses, and satel-

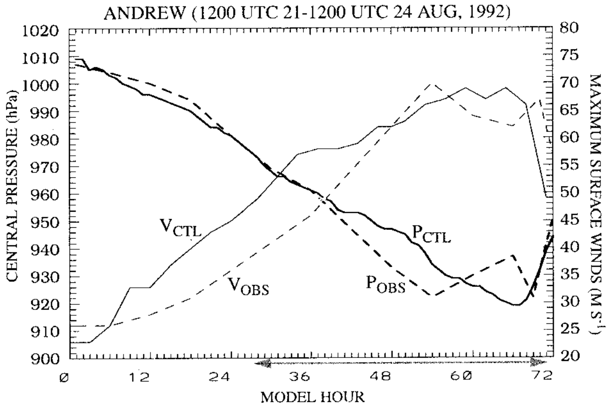

FIG. 2. Time series of the minimum central pressures P (hPa) and the maximum surface winds V (m s^{-1}) of Hurricane Andrew from the 72-h simulation (P_{CTL} and V_{CTL}) and the corresponding best analysis (P_{OBS} and V_{OBS}) by Mayfield (1994). The arrow along the abscissa shows the period of integration for the 6-km mesh.

lite and radar imagery). The next section will be devoted to the examination of some detailed structures in the central-core region of Hurricane Andrew.

Figure 1a compares the tracks of Hurricane Andrew between the simulation (from the hourly model output) and the 6-h best analysis of Mayfield et al. (1994). The observed storm moved west-northwestward in the first 24 h and then nearly straight westward, whereas the simulated storm propagates westward first, followed by a west-northwestward displacement. Furthermore, the simulated hurricane translates a little faster than the observed in the first 12 h and slower in the last 12 h. The errors in both the direction and movement account for the maximum track deviation of 250 km at 18 h. These errors are likely caused by (i) the insufficient information in the large-scale initial conditions, particularly for the newly formed favorable environment, which are responsible for the observed curvature of the storm; and (ii) the incorporation of the model-generated vortex into the initial conditions that may distort somewhat the interaction of the storm with its larger-scale environment. Nevertheless, after 1-day spinup, the large-scale flow, reasonably represented by the NCEP analysis, appears to steer the vortex nearly along the right track with the right speed. On the average, the storm translates at a speed of 6–8 m s^{-1}. Thus, the deviation in track decreases to nearly null at 48 h, and increases only slightly afterwards, with an error of less than 100 km at the time of landfall. The accurate prediction of the track during the final 2 days appears instrumental in the successful simulation of Andrew's rapid development, considering that the storm interacts strongly with the warm SST anomalies over the straits of Florida and the underlying orography during landfall.

To demonstrate the model's capability in reproducing the explosive deepening of Hurricane Andrew from the initial conditions generated by the NCEP analysis, we compare in Fig. 2 the time series of the minimum central pressure and the maximum surface winds between the simulation and the best analysis. Although the simulated details differ somewhat from the analysis, the general comparison of their trends is favorable. For example, the model reproduces very well the rapid deepening rate of central pressure ($>$1.5 hPa h^{-1}) and the steady increase of surface winds during the first 36 h. Note that during the first 27 h, this rapid deepening is primarily produced by parameterized deep convection over the mesh B domain. Activating the finest mesh C at 27 h does not seem to cause significant immediate impact on the deepening rate. However, it may account for the reduced deepening rate between the 36- and 54-h integrations compared to the observed, owing to the inherent adjustment taking place in the model. The storm reached a minimum central pressure (P_{OBS}) of 922 hPa twice preceding landfall in Florida: the first at 1800 UTC 23 and the other just prior to landfall. In contrast, the simulated hurricane continued its intensification to a minimum central pressure (P_{CTL}) of 919 hPa near landfall. This discrepancy may be caused by a double-eyewall cycle leading to the temporary weakening of the storm (Willoughby and Black 1996). This process does not seem to be duplicated by the model, owing likely to the use of imperfect initial conditions and of the 6-km resolution being too coarse to resolve the detailed contraction processes. It should be mentioned that the simulated maximum intensity preceding landfall could not be obtained without incorporating realistic model physics, an issue which will be discussed in a forthcoming article.

While the model reproduces the observed deepening of Hurricane Andrew in the first 36 h, the simulated maximum surface winds (V_{CTL}) are 5–8 m s^{-1} higher than the analyzed (V_{OBS}) from 12 to 42 h. This could be attributed partly to the use of surface observations at different locations from those in the model and partly to the different resolutions between the observations and the simulation in capturing the maximum winds. Nonetheless, the model is able to deepen the storm from tropical storm intensity (i.e., $V_{\max} > 20$ m s^{-1} at the surface) to category 1 intensity ($>$33 m s^{-1}) in 12 h, category 2 ($>$41 m s^{-1}), category 3 ($>$48 m s^{-1}), and category 4 ($>$57 m s^{-1}) intensities in 20 h, 28 h, and 36 h, and finally to a near–category 5 hurricane ($>$68 m s^{-1}) intensity near the Bahamas. The simulated maximum surface wind during the mature stage is only 1 m s^{-1} weaker than the observed. Unlike the central pressure traces, the maximum surface winds from the model do show two peaks during the mature stage, albeit at a timescale much shorter than that in the analysis. The model also mimics very well the abrupt decrease of the maximum surface winds during Andrew's landfall.

It is well known that the predictability of the track and intensity of a hurricane presented above depends on the generation of realistic larger-scale environmental conditions, such as static stability (Krishnamurti et al. 1991), moisture content (Kurihara 1985), and wind

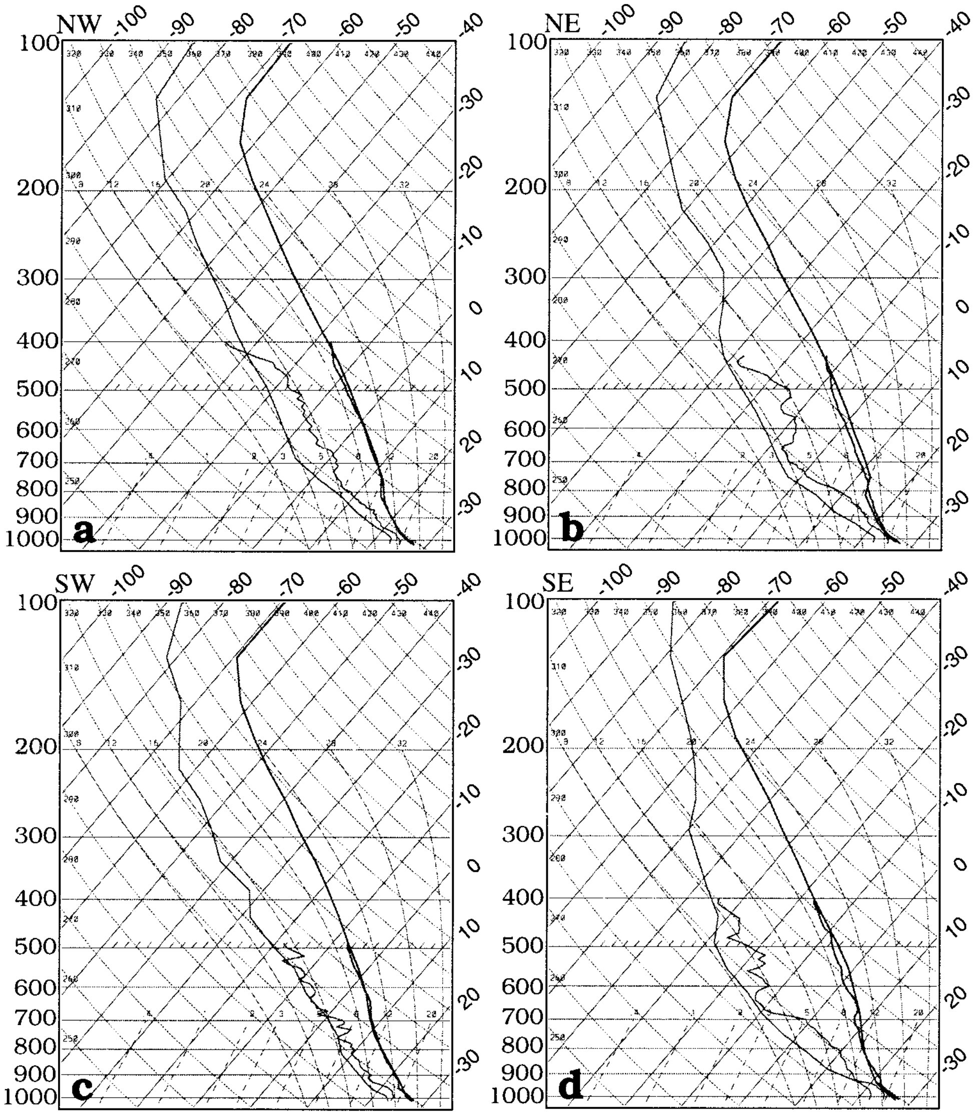

FIG. 3. Comparison of composite soundings between the simulation (up to 100 hPa) and ODWs (released at 400 hPa) in the (a) northwest (NW), (b) northeast (NE), (c) southwest (SW), and (d) southeast (SE) quadrants of Andrew for the period centered at 0000 UTC 23 August 1992.

shears (Gray 1979) in the lower troposphere. Thus, it is desirable to examine if the generated ''model atmosphere'' would conform to the real atmosphere or if the results presented are obtained for the right reasons. Fortunately, during the rapid developing stage of Andrew (i.e., from 1800 UTC 22 to 0300 UTC 23 August), NOAA's two reconnaissance aircraft released a total of 49 ODWs at the 400-hPa level with an average interval of 150 km over a 150 × 150 (latitude–longitude) area across the storm. For the purpose of model verification, 49 soundings from mesh A at nearly the same location as the ODWs are sampled from the 36-h integration. Then, a composite sounding for each quadrant is computed and compared in Fig. 3 to the observed.

It is apparent that the model favorably reproduces the observed thermal structure up to 400 hPa in all quadrants (see Figs. 3a–d). In both the simulation and the observations, intense sensible heat flux from the warm ocean produces in the lowest 50–80 hPa a well-mixed boundary layer. The model soundings also exhibit the relatively moist troposphere below 800 hPa and drier air above, separated by a weak inversion. However, the simulated moisture content appears to be systematically drier than the observed (near saturation), although the drying is much less notable in the upstream quadrants (see Figs. 3a,c). As noted by Franklin et al. (1988), the near-saturated boundary layer in the ODWs could be attributed to instrument errors as they were dropped rapidly through stratocumulus clouds in the vicinity of the storm. Therefore, the large-scale environment in

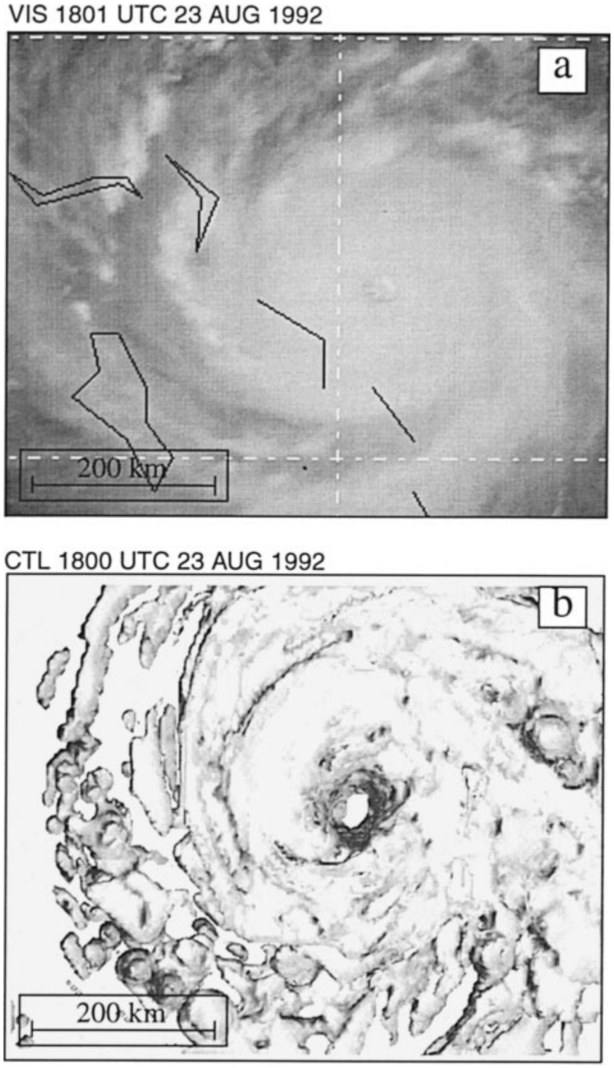

FIG. 4. (a) Visible satellite imagery at 1801 UTC 23 August 1992 and (b) a top view of the model-simulated hydrometeors, as determined by the 0.01 g kg^{-1} surfaces for cloud water and ice, rainwater, and snow, and graupel, from 54-h simulation (valid at 1800 UTC 23 August 1992). Both panels cover the same area.

which Hurricane Andrew is embedded can be regarded as being realistically simulated; this is again attributable to the modified NCEP analysis in the absence of upper-air observations over the ocean and to the use of the Blackadar high-resolution boundary layer scheme and the Betts–Miller shallow convective adjustment scheme. The above results may not be so surprising since they have more or less been obtained in previous studies (see the references given in section 1).

Now let us shift our attention to the verification of the system-scale features, such as the cloud and flow fields. Figure 4a displays a visible satellite imagery at the mature stage of the hurricane, while Fig. 4b shows a top view of the hydrometeors fields as delineated by the 0.01 g kg^{-1} isosurfaces of cloud water and ice, rainwater, snow, and graupel from the 54-h simulation. Very interestingly, the simulated general cloud distribution and the area of the storm conform well to the satellite imagery. Both the model and the observations show the development of organized spiral cloud bands with an echo-free eye in its central core. Although it is not possible to predict the detailed distribution of convective cells along the spiral bands, the model does simulate well the cellular convection at the outer edge and the intense and organized (convective and stratiform) clouds in the eyewall. In general, the evolution of these cloud features in the simulation also compares favorably to the satellite observations at different stages of Andrew (not shown).

The isosurfaces of hydrometeors described above could only provide a top view of the storm. The simulated radar reflectivity, on the other hand, indicates how well the model predicts the precipitation field and the rainfall rate. In the present case, the structure of the storm at landfall was well captured by the Miami WSR-57 radar. Figure 5a displays the reflectivity (dBZ) of the last scan of the radar before it was destroyed by the violent winds. For the purpose of verification, the model radar reflectivity is estimated using the relation between reflectivity Z ($mm^6\ m^{-3}$) and rainfall rate R ($mm\ h^{-1}$) as

$$\mathrm{dB}Z = 10 \log_{10} Z, \tag{1}$$

where

$$Z = 300R^{1.35} \quad \text{(rainwater)}, \tag{2}$$

and

$$Z = 427R^{1.09} \quad \text{(ice particles)}. \tag{3}$$

Equations (2) and (3) were taken from Jorgensen and Willis (1982) and Fujiyoshi et al. (1990), respectively. (Contribution of cloud water to reflectivity is small and therefore neglected.) In addition, a correction factor of 4.46 is applied wherever melting ice particles are present (Smith 1984). We found that the simulated reflectivities above the melting level seem to be systematically stronger than the observed, roughly by 5 dBZ. Nevertheless, it is encouraging that the model reproduces very well the echo-free eye with a radius of 9–12 km at the coast of Florida (Fig. 5b). Also well reproduced is the intense precipitation along the eyewall as denoted by radar reflectivity greater than 50 dBZ and the cellular deep convection embedded in the spiral rainbands, particularly in the trailing spiral stratiform region to the east. High radar reflectivities of greater than 50 dBZ, corresponding to a rainfall rate of greater than 65 mm h^{-1}, are also depicted in the region of the trailing spiral rainband as they are locally generated by deep convection. Note that all of these features are highly asymmetric. Note also that the simulated eyewall is more intense over land, a feature consistent with observations from the Key West radar at 0902 UTC 24 August (see Fig. 12 in Wakimoto and Black 1994). Wakimoto and Black noted that the

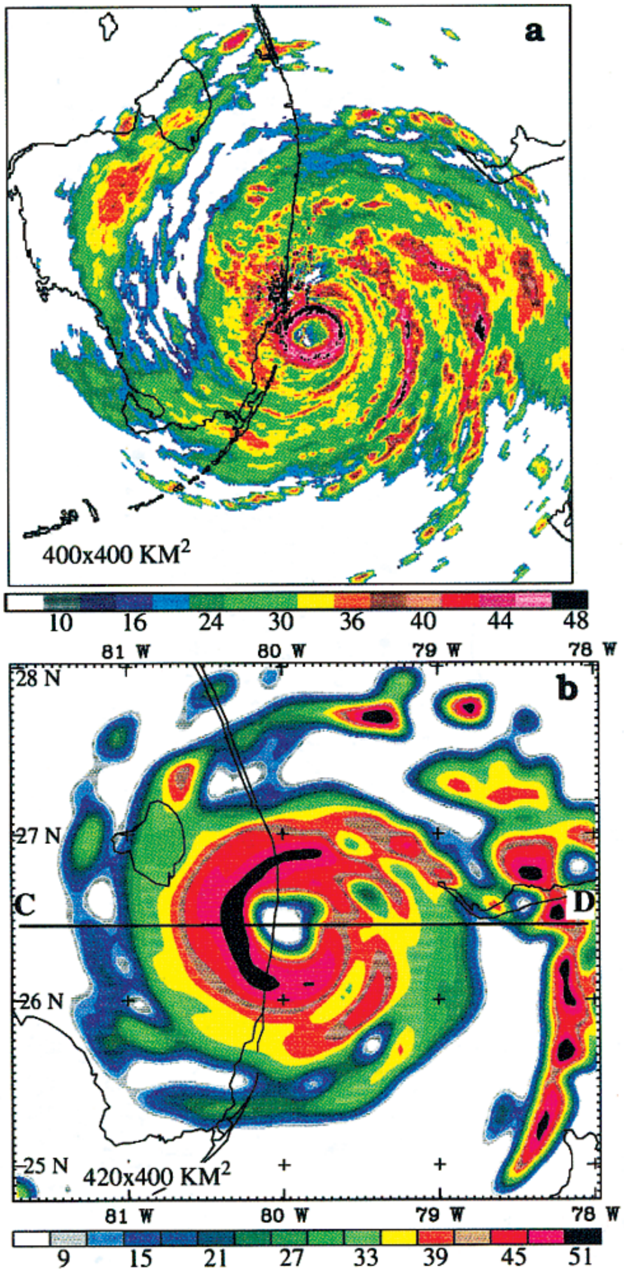

FIG. 5. (a) Radar reflectivity from the Miami WSR-57 radar at 0830 UTC 24 August 1992 and (b) the simulated reflectivity that is taken from 68-h integration valid at 0800 UTC 24 August 1992. The legend given along the abscissa denotes the intensity of reflectivity in terms of dB*Z*. The intervals marked on the frame are mesh grids (6 km for the finest mesh, similarly in the rest of figures).

more intense deep convection in the eyewall developed in the northwest quadrant and then moved into the southwest quadrant as Andrew reached the coast of Florida. They speculated that the intense convective development is mainly caused by the stronger convergence forced by the larger friction over land.

Although the model reproduces most of the significant cloud features, a detailed comparison with the radar observations in Wakimoto and Black (1994) shows two notable deficiencies with the simulation. First, the simulated eyewall, 18–24 km *in width*, nearly doubles the observed. Because of this deficiency, the radius of the model eyewall is twice larger than the observed. This is clearly due to the fact that the model with a 6-km grid spacing cannot produce intense convective cells on a scale of a few kilometers in the eyewall. Second, the calculated surface reflectivity seems to indicate that the model does not reproduce the intense squall line along the west coast of Florida during the final few hours of integration (cf. Figs. 5a,b); although the upper-level reflectivities do exhibit a spiral cloud band coinciding with the system (not shown). Examination of the time sequence of the satellite imagery reveals that the squall line is a rapid-moving, shorter-lived convective system ahead of the hurricane. Nonetheless, the surface reflectivities, given in Figs. 6a–c, do show the generation of the squall-line convection prior to landfall, albeit less organized. The simulated squall line spreads from the eyewall, like a spiral rainband ahead of the hurricane (Fig. 6b). Its movement is determined by the westward displacement of the hurricane, the cyclonic rotation of the line convection with respect to the eye, and the inward propagation of convective cells along the line. Apparently, the squall line dissipates at a time earlier than the observed (cf. Figs. 6c and 5b) as it rotates cyclonically into central Florida where it may encounter an unfavorable environment.

Figures 6a–c also depict several features that fit the conceptual description of a hurricane. Specifically, Willoughby et al. (1984b) classified the hurricane rainbands into eyewall, principle, secondary, and connecting rainbands. They are all well simulated by the model, particularly at the most intensifying stage (see Fig. 6a). Evidently, it is the rainband at the outer edge that tends to develop into the squall line in the present case. As Andrew moves over land (i) the eye begins to fill, (ii) the eyewall expands in size, and (iii) the radar reflectivities or the rainfall rates weaken rapidly (cf. Figs. 6b,c). All these features are qualitatively consistent with those from previous studies of hurricanes.

Figure 7 compares the simulated surface winds to the observational analysis of Powell and Houston (1996) at the time of landfall. The analysis was obtained by compositing all available wind observations including both flight level and surface (at an elevation of 10 m) measurements over land and near shore for a time window of 6 h between 0430 and 1030 UTC 24 August. It is encouraging that the model reproduces very well the development of the RMW with winds greater than 55 m s^{-1}, the asymmetry of the RMW with respect to the center of the eye (e.g., 22 km in the southwest quadrant versus 40 km in the northwest quadrant), the marked cyclonic confluence of streamlines into the central core and weak winds in the eye. In particular, the model reproduces almost perfectly the strongest surface winds

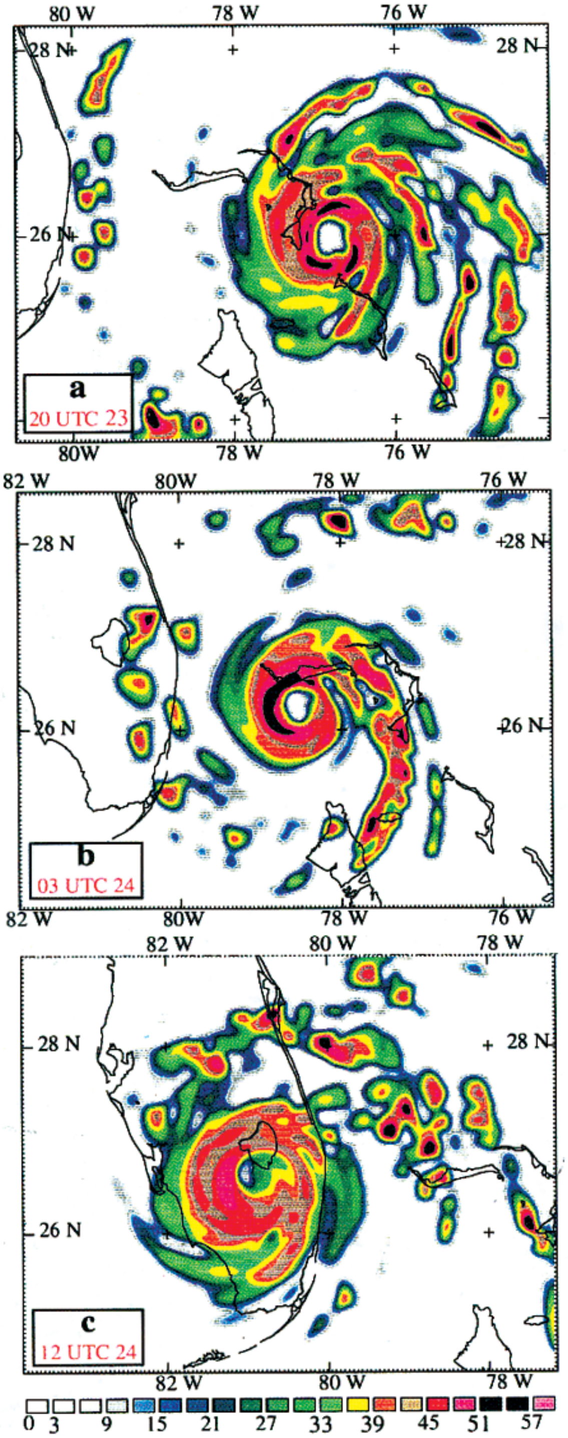

FIG. 6. Time evolution of the radar reflectivity at the surface (i.e., $\sigma = 0.995$) from the final 16-h integrations of Hurricane Andrew (i.e., from 2000 UTC 23 to 1200 UTC 24 August 1992).

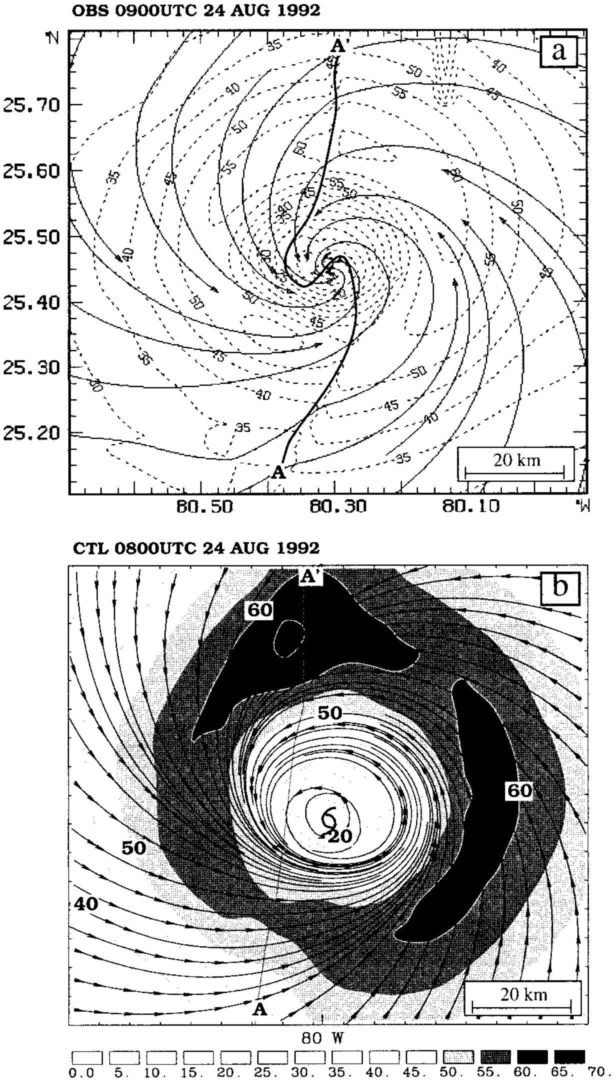

FIG. 7. Comparison of surface streamlines and wind speeds at intervals of 5 m s^{-1} between (a) the surface composite [adapted from Powell and Houston (1996)] and (b) the simulation at landfall of Hurricane Andrew; both are displayed over a similar domain. Curve *AA′* marks the east coast of Florida in the simulation and the boundary between over land and over water exposures in the analysis.

of greater than 65 m s^{-1} to the north of the eye at the shoreline. The difference from the analysis is less than 1.5 m s^{-1}. The development of the strongest winds in the presence of intense surface friction as Andrew moved farther inland has also been noted by Wakimoto and Black (1994). It is found from the model simulation that this strong-wind zone coincides with the generation of local intense precipitation, as can be indirectly inferred from Fig. 5b. Thus, the strongest-wind zone near the coastline to the north results from the intensified deep convection, which is in turn attributable to the rapid increase in surface friction and the enhanced low-level convergence of mass and moisture (Parrish et al. 1982; Burpee and Black 1989). It should be noted that

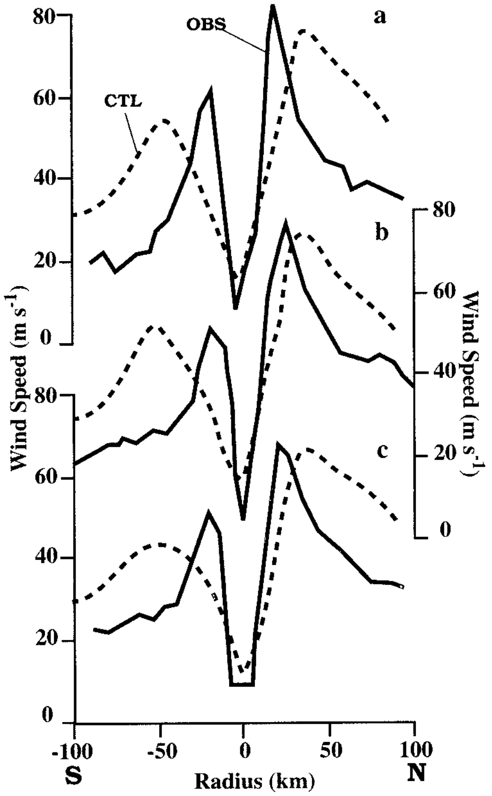

FIG. 8. Comparison of the south–north wind profiles between the aircraft observations [solid, reproduced from Willoughby and Black (1996)] and the simulation (dashed) (a) an hour before landfall, (b) at landfall, and (c) an hour after landfall.

the large discontinuity in surface winds along the coastline in the Powell–Houston analysis was mainly caused by converting the flight-level data using their boundary layer model over land and ocean, separately, and then merging them along the coastline without including full dynamic and physics interactions.

While the model reproduces well the magnitudes and structures of the RMW, its radius, like that of the eyewall, appears to be overpredicted. This could be more clearly seen from Fig. 8, which shows the wind speed in a south–north direction at times prior to, at, and after landfall. The error in radius is 10–15 km for the stronger winds along the RMW to the north, but it is 30 km for the weaker winds to the south. The strength of the general flows outside the RMW are also overpredicted. Nevertheless, the basic flow pattern within the eye and the intense wind shear northward from the center are well reproduced (e.g., see Fig. 7).

In summary, we may state that despite some deficiencies with the simulation, the model reproduces reasonably well the track, the intensity, the eye, the eyewall, the spiral rainbands, the RMW, and the landfall of Hurricane Andrew, as verified against numerous observations. Such encouraging predictability will be shown in the forthcoming articles to result from the use of realistic model physics and the specification of the right vortex at the model initial time, given the reasonable NCEP analysis and the SST field. Therefore, in the next section and forthcoming articles, we may use the model results with confidence to provide an understanding of various elements and physical processes involved in the rapid deepening of Hurricane Andrew or other tropical storms, if their precise timings and locations are of lesser concern.

5. Vertical structures

In this section, we compare some of the vertical structures of the simulated Andrew to those reported in previous studies. For economy of space, we will focus only on the mature stage of the storm (i.e., at 2000 UTC 23 August 1992), since tropical cyclones at all geographic locations show great similarity in structure and organization at the mature stage.

To assess the capability of MM5 in simulating the inner-core structures of Andrew, we show in Figs. 9 and 10 the vertical structures of model-simulated radar reflectivity associated with the storm. It is interesting to note that as in nature, the model is able to mimic the increase in scale of the eye with height, that is, from 16 km in diameter near the surface to about 80 km at 200 hPa (Figs. 10a,b). Various types of spiral rainbands as described by Willoughby et al. (1984b) are also evident, but with pronounced variabilities and asymmetries across the storm (Marks 1985), even in the region of the eye (Fig. 9). Of further interest is that the spiral rainbands, as well as the eyewall, tend to merge (in terms of cloud particles) with their neighboring rainbands upward; so wider and more homogenous rainbands, albeit fewer in number, appear higher up (Figs. 9a–c). This is particularly true in the upper regions marked by divergent outflow (cf. Figs. 10, 15, and 16), where the echo intensity decreases outward (Fig. 9a) but still with stronger precipitation concentrated in the eyewall. All these features resemble well airborne radar observations in other hurricanes (e.g., see Fig. 1 in Jorgensen 1984b; Fig. 8 in Marks 1985; Fig. 6 in Houze et al. 1992).

The vertical cross sections (Figs. 10a,b) also depict higher values of radar reflectivity below 650 hPa and a rapid decrease above, which are indicative of the effect of intense melting across the 0°C isotherm. The highest reflectivity (>50 dB*Z*) is always located in the eyewall, with sharp gradients at its inner edge. This feature is consistent with the often observed intense convection and heavy precipitation in that region. Note that the eyewall at the mature stage is more symmetric than that at landfall (cf. Figs. 5b and 9c). This difference appears to reflect the presence of different surface forcings, that is, over the relatively uniform ocean versus along the coastline. Note also that the eyewall slopes radially outward with height. According to radar observations (Jorgensen 1984a; Marks 1985; Houze et al. 1992; Roux

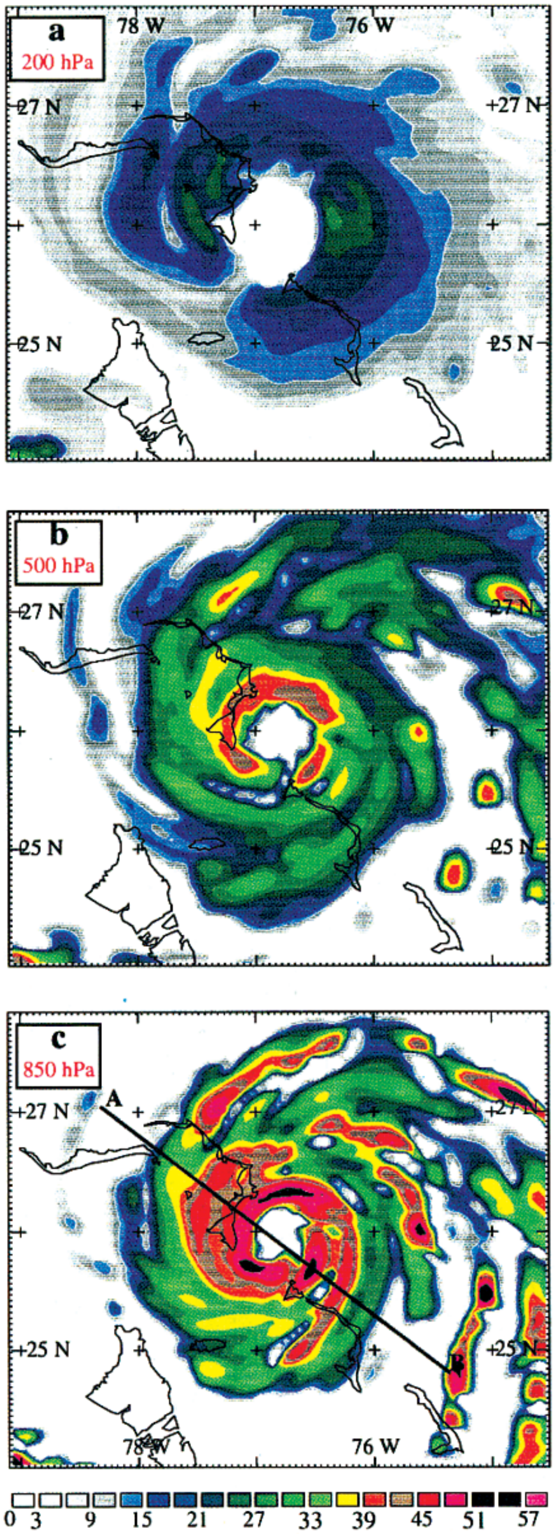

FIG. 9. Horizontal distribution of the model-simulated radar reflectivity at (a) 200, (b) 500, and (c) 850 hPa, which are taken from 56-h integration, valid at 2000 UTC 23 August 1992.

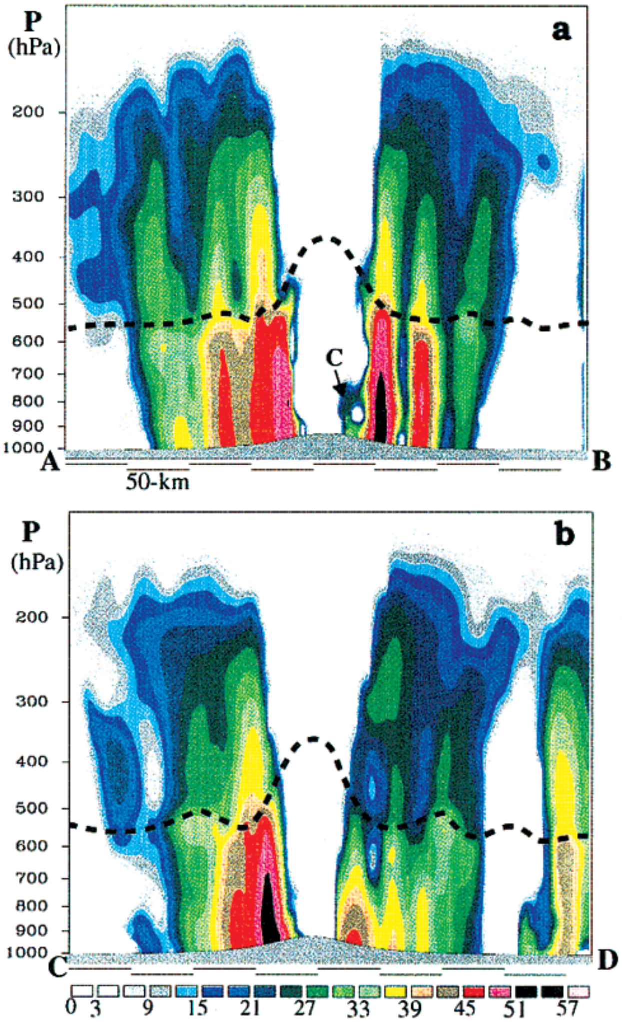

FIG. 10. Vertical cross sections of the simulated radar reflectivity that are taken, respectively, along line *AB* in Fig. 9c and line *CD* in Fig. 5b from (a) 56-h and (b) 68-h integrations, valid at 2000 UTC 23 and 0800 UTC 24 August 1992. Dashed black line denotes the 0°C isotherm. Each horizontal bar along the abscissa denotes a distance of 50 km and the width of the sections is 415 km.

and Viltard 1995), the inner slope of the eyewall, measured by the orientation of the 10-dB*Z* contour, normally spans from 1:1 to 1:2, or from 45° to 30° with respect to the horizontal axis. In the present case, the model-generated slopes range from about 1:1 at 2000 UTC 23 (Fig. 10a) to 1:3 at 0800 UTC 24 August (Fig. 10b). The reduced slope preceding landfall is accompanied by the low-level contraction of the eyewall (cf. Figs. 10a,b) as the storm deepens rapidly (see Willoughby et al. 1982). The shallow cloud mass in the eye region, marked by ‘‘C,’’ is a transient feature, and it appears to be associated with the contraction process that tends to advect hydrometeors across the RMW (or the ‘‘broken eyewall’’) into the eye region (cf. Figs. 9c and 10a) under the influence of the horizontal pressure gradient force.

Figures 11a–c show how the different cloud microphysical quantities, that is, rainwater, cloud ice, snow, and graupel, contribute to the generation of the reflectivity structures discussed above. The distribution of cloud water is also plotted. One may note that the large regions of weak-reflectivity at the outer edge are covered by cloud ice and snow with mixing ratios much less than 0.1 g kg^{-1}. It is apparent that the model reproduces reasonably well the distribution of supercooled water and solid (liquid) particles above (below) the 0°C isotherm or the melting/freezing level. Again, the more significant precipitation particles, both solid and liquid, are concentrated in the eyewall, with little cloud water in the eye. Because cloud water and ice have negligible fall velocity, they are carried mainly by updrafts and sloped outward with height in the eyewall. The cloud base is located near 500 m but most of the cloud water develops near the 800-hPa level, where tremendous condensation occurs in the eyewall. In contrast, rainwater/snow and graupel contents tend to be vertically distributed as these particles fall through a column faster than the timescale for horizontal advection.

In the ascending region, cloud ice is initiated through nucleation and freezing of supercooled water, and subsequently grows by deposition. These production terms lead to high concentrations of cloud ice near 300 hPa (Fig. 11a). Because snow forms as cloud ice reaches a critical size where aggregation and riming become important, it is closely related to the cloud ice content and tends to have a maximum in the 300–200-hPa layer where depositional growth dominates (Figs. 11a,b). Snow appears to be responsible for the generation of large and deep anvil regions aloft. Similarly, snow begins its conversion to graupel as its size exceeds a critical value. Graupel grows very fast by collecting liquid and solid particles along its path (Fig. 11c). It then melts into rain as it falls through the level of the 0°C isotherm. As a result, the peak mixing ratios tend to be largest for rainwater (4–6 g kg^{-1}), followed by graupel (2–4 g kg^{-1}), cloud water (0.8–2.0 g kg^{-1}), cloud ice (0.8–1.2 g kg^{-1}), and snow (0.5–0.8 g kg^{-1}), in that order. These microphysical processes, their vertical distributions, and magnitudes are all in good agreement with in-situ microphysics observations (Black and Hallett 1986; Houze et al. 1992) and airborne Doppler radar data (Marks and Houze 1987) in other hurricanes. Our results show clearly the importance of including ice microphysics in generating more realistic cloud structures in a model hurricane, in agreement with the finding of Willoughby et al. (1984a) and Lord et al. (1984).

To gain insight into the generation of the extremely low pressure at the center, Fig. 12 presents a vertical cross section of deviation temperature at the mature stage. (The deviation temperature is obtained by subtracting the temperature from the pressure-level average.) A marked warm-core structure from the surface to the tropopause is evident in the eye region, with little net warming outside the eye in spite of the intense latent

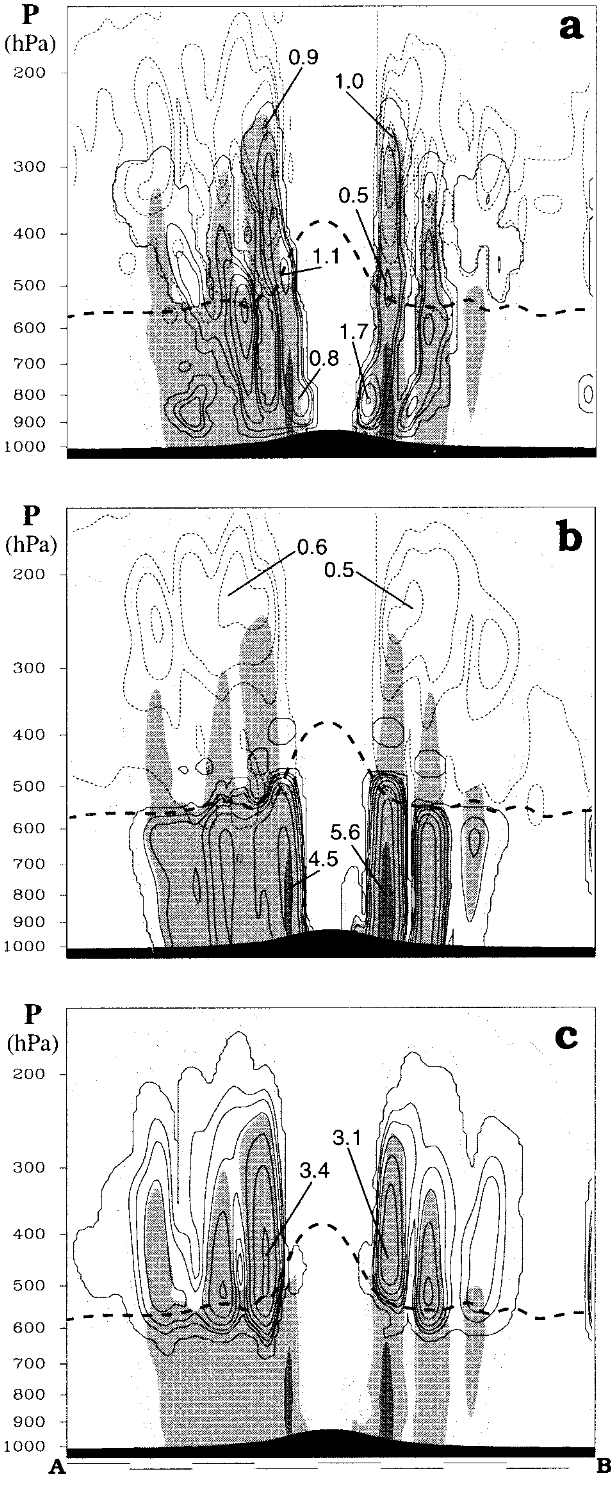

FIG. 11. As in Fig. 10a but for the mixing ratios of (a) cloud water/ice (solid/dashed), (b) rainwater/snow (solid/dashed), and (c) graupel at isopleths of 0.001, 0.1, 0.2, 0.4, 0.8, 1.6, 3.2, and 6.4 g kg^{-1}. The simulated radar reflectivity is superposed with gray scales. Thick solid line denotes the distribution of the 0°C isotherm.

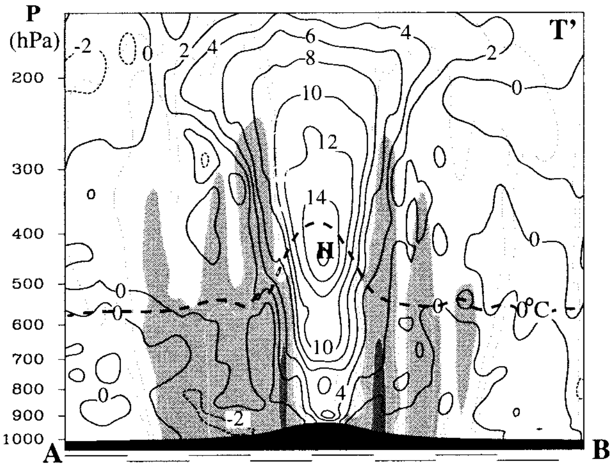

FIG. 12. As in Fig. 10a but for the temperature deviation at intervals of 2°C. Solid (dashed) lines are for positive (negative) values. The simulated radar reflectivity is superposed with gray scales. Thick solid line denotes the distribution of the 0°C isotherm.

heat released, for example, in the eyewall and the spiral rainbands. The general feature of the warm core is very similar to the multilevel flight observations in (also compact) Hurricane Inez (1966) (see Hawkins and Imbembo 1976). Apparently, diabatic heating in these regions is mostly compensated by adiabatic cooling associated with the intense ascent. Like the eye, the horizontal extent of the warm anomaly also expands in diameter with height, with a sharp thermal gradient sloping along the eyewall except in the upper-level (outflow) anvil region. The maximum temperature anomaly is 16°C over a distance of 75 km near 500 hPa, which is about 2°C larger in magnitude but 200 hPa lower in altitude than those obtained in an idealized hurricane simulation (having a smaller eye) by Kurihara and Bender (1982) and a theoretical estimate of intense hurricanes by Emanuel (1986). The large amplitude of warming in the eye may partly explain why Andrew is much more intense than other hurricanes. One can also note the presence of net cooling (>2°C) below the melting level outside the eyewall, indicating the possible cooling effect by melting and evaporation in mesoscale downdrafts (Gamache et al. 1993).

Figure 13a shows a vertical cross section of the equivalent potential temperature θ_e. This quantity is used here as a tracer to help understand the thermodynamic structure and the origin of different air masses, since it represents the static energy of air parcels and is conserved in an inviscid, pseudoadiabatic flow. Several important features could be noted. First, as an air parcel in the PBL flows inward from the outer high pressure region, its θ_e increases rapidly as a result of the air–sea interaction (Rotunno and Emanuel 1988) by the upward transfer of sensible and latent heat fluxes from the underlying warm ocean. Over a distance of 100 km toward the center, the θ_e increases by 25 K! According to the empirical estimation of hurricane intensity by Malkus and Riehl (1960), that is, using the equation of $P_{\mathrm{sea}} - 1000 = -2.5(\theta_{e\,\max} - 350)$, the simulated $\theta_{e\,\max}$ of 382 K at the center would produce a minimum pressure of 920 hPa, which is close to the simulated 919-hPa value (cf. Figs. 13a and 2). Second, intense vertical gradients of θ_e occur at the top of the maritime boundary layer, with minimum θ_e values near 700 hPa. Such strong θ_e gradients result mostly from the radiative cooling at the top of stratocumulus clouds, which tends to produce more potentially unstable conditions for the development of deep convection and for the deepening of hurricanes (Krishnamurti et al. 1991). Third, the central core is characterized by high-θ_e air that is extremely warm but dry. The lower-θ_e air centered at 600 hPa in the eye, which has also been observed by Hawkins and Imbembo (1976) and Jorgensen (1984b), is mainly due to its extreme dryness. The high-θ_e air above 400 hPa

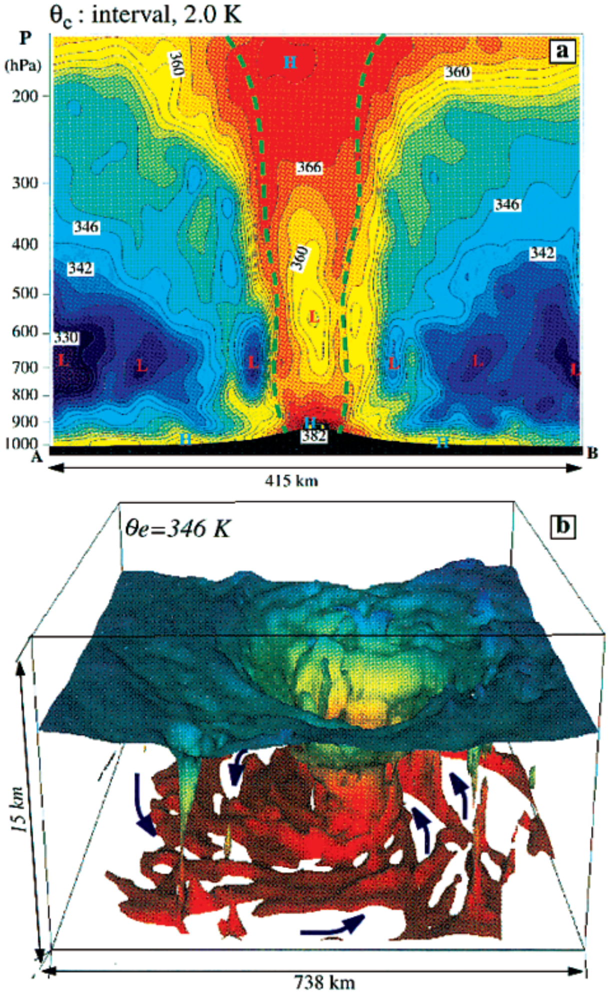

FIG. 13. (a) As in Fig. 10a but for the equivalent potential temperature θ_e at intervals of 2 K and (b) a three-dimensional view of θ_e = 346 K surface over mesh C domain. In (a), different θ_e regions are colored from yellow (warm) to blue (cold) and dashed green lines show the eyewall as defined by the radar reflectivity of 10 dBZ.

appears to descend from the tropopause, whereas below 800 hPa it is generated by the upward transport of surface fluxes. Fourth, note the marked downward dip of higher-θ_e values at the inner edge of the eyewall that suggests the presence of stronger descending motion near the edge, as will be shown in Fig. 15. All these structures are in good agreement with those revealed by aircraft observations of other hurricanes (Hawkins and Imbembo 1976; Jorgensen 1984b).

A 3D view of the $\theta_e = 346$ K surface over the mesh C domain is given in Fig. 13b, which clearly shows the distribution of the various features associated with the eye, the eyewall, and the spiral rainbands. In particular, one can see that the spiral bands attain high-θ_e air from the underlying ocean and then transport it into a deeper layer as the bands rotate toward the eyewall. At some locations where deep convection is intense, penetrative high-θ_e columns between the surface and the tropopause form, thereby transporting higher-θ_e air into the upper troposphere.

At this point, it is of interest to examine how the model-simulated soundings in the eye and eyewall compare to those observed, since they are in dramatically different environments. It is evident from Fig. 14a that the sounding in the eye is extremely dry between 500 and 200 hPa; its minimum relative humidity reaches 5% as a result of intense subsidence in the core. A shallow moist layer with high θ_e occurs in the lowest 200 hPa (cf. Figs. 14a and 13a) with an intense thermal inversion above. This inversion separates the descended dry air of an upper-level origin from the moist air in the PBL. Diagnostic analysis of the model output shows that although the thermal inversion and dryness in the eye could change substantially from time to time, the basic structure of ‘‘upper-dry’’ and ‘‘bottom-moist’’ is always present. This sounding and its associated large variations resemble well those dropsonde observations in other hurricanes (e.g., Frank 1977; Franklin et al. 1988).

In contrast, the eyewall sounding exhibits a near-saturated thermal structure up to 500 hPa, with a well-mixed boundary layer below and a subsaturated layer above (see Fig. 14b). As expected, the temperatures throughout the troposphere are systematically much colder than those in the eye (cf. Figs. 14a,b and 12); a thermal gradient of 12°C per 66 km is seen at the top of the well-mixed boundary layer. Note the generation of a sub-moist-adiabatic and saturated layer below the 0°C level (at 540 hPa), which is found to result mainly from the melting of tremendous amount of graupel and snow as they fall through the layer (cf. Figs. 11 and 14b). A similar thermal structure appears above 500 hPa, but it is more closely associated with the system's outflow of drier and warmer air from the core. Thus, the upper troposphere in the eyewall is relatively drier than in the lower layers. These sounding structures have also been more or less observed (Frank 1977; Hawkins and Imbembo 1976).

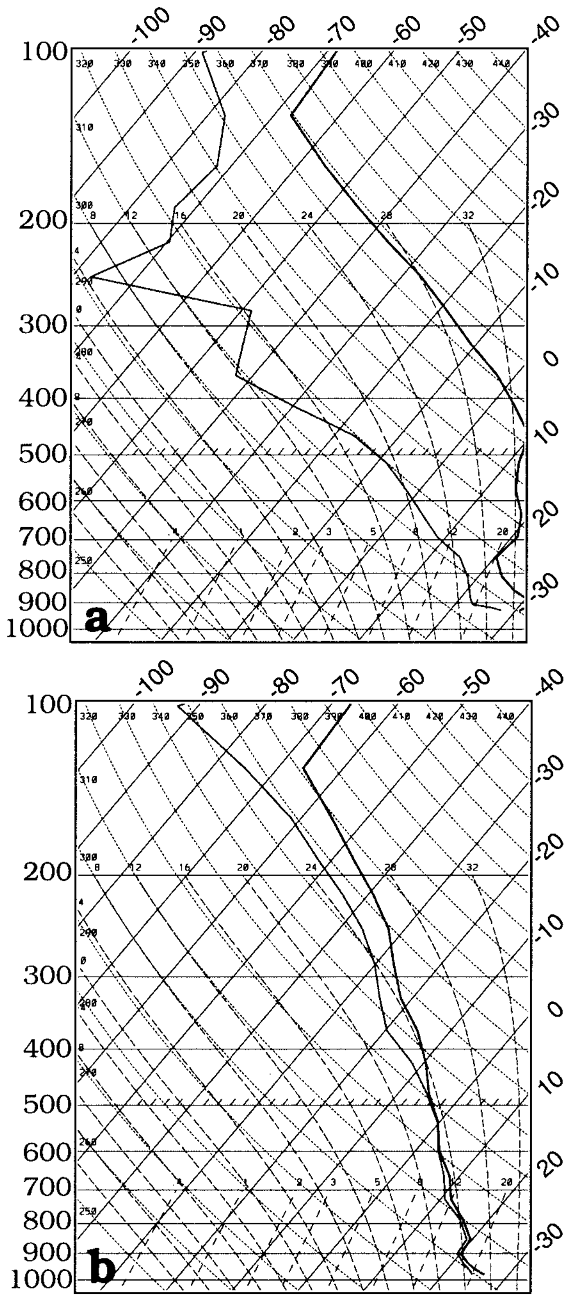

FIG. 14. As in Fig. 10a but for the simulated soundings (a) at the center (i.e., with the minimum surface pressure) and (b) in the eyewall (about 66 km to the east from the center).

Finally, we examine the simulated 3D flow fields in the vicinity of Hurricane Andrew during its mature stage. The vertical cross section of tangential winds (Fig. 15a) shows the existence of the RMW throughout the troposphere in the eyewall, with isotachs tilting outward with height, like the radar reflectivity. This structure conforms to the observational analyses of other hurricanes (e.g., Marks and Houze 1987; Marks et al. 1992) and theoretical studies (e.g., Shapiro and Willoughby 1982). As also found in previous studies, there

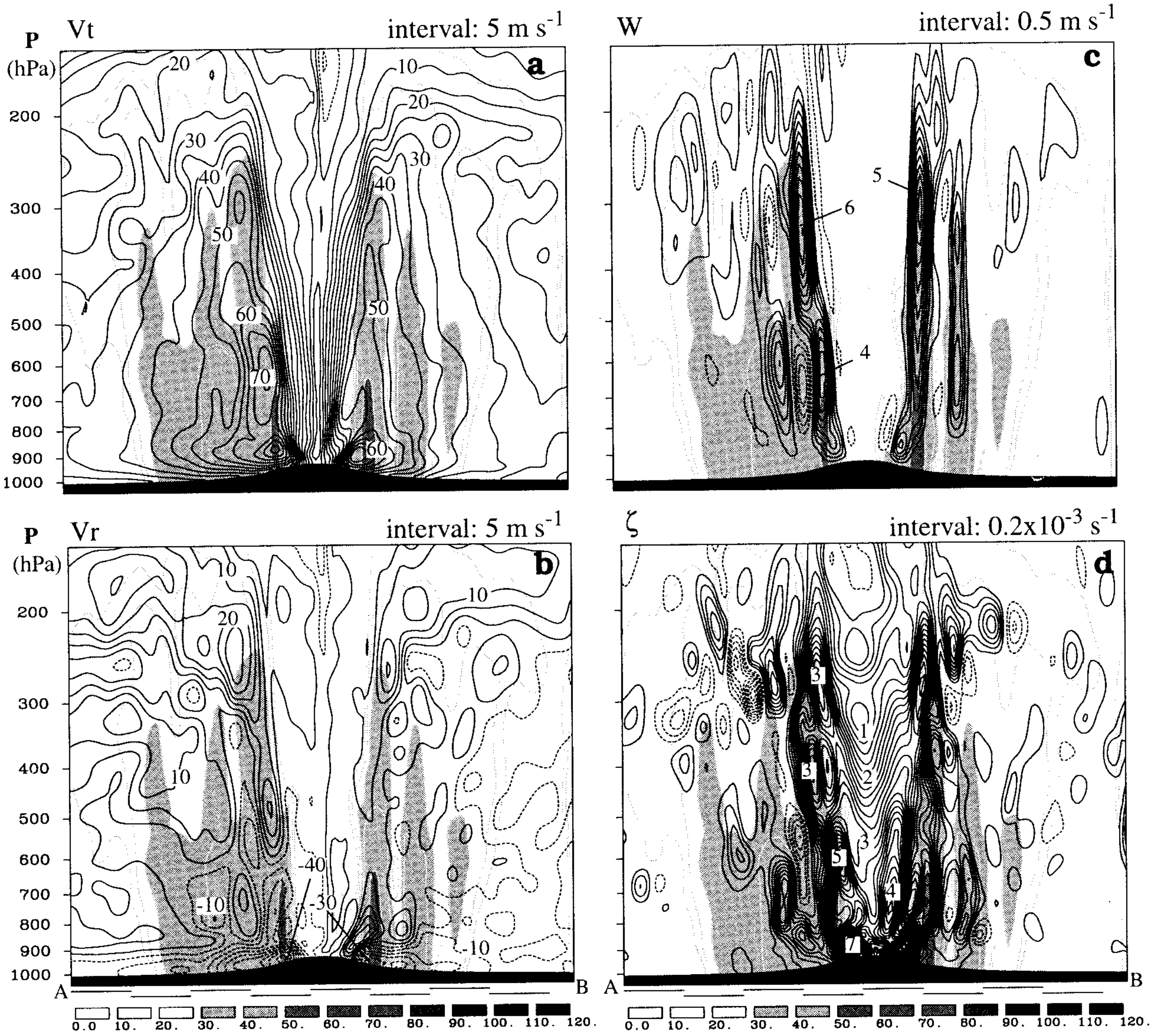

FIG. 15. As in Fig. 10a but for (a) tangential winds V_t (every 5 m s^{-1}), (b) radial winds V_r (every 5 m s^{-1}), (c) model-output vertical velocity w (every 0.5 m s^{-1}), and (d) vertical relative vorticity ζ (every 0.5 × 10^{-3} s^{-1}). Solid (dashed) lines are for positive (negative) values.

are two or more wind maxima (>75 m s^{-1}) in the vertical (e.g., Franklin et al. 1993): one roughly at 900 hPa and the other near 700 hPa; their magnitudes decrease sharply upward. The peak in the wind at the lower levels is a consequence of the partial conservation of angular momentum as air parcels swirl rapidly inward against the surface friction. The upper-level maximum is generated partly by vertical advection of angular momentum and partly by latent-heat-induced acceleration in the eyewall. The strongest wind of 87.5 m s^{-1}, which occurs near 900 hPa just before landfall over Florida, is close to the in situ observations of 85 m s^{-1} at 700 hPa by reconnaissance aircraft at this time (Mayfield et al. 1994).

In general, radial winds (Fig. 15b) exhibit strong inflows in the lowest 100-hPa boundary layer and intense outflows above 300 hPa, with relatively weak and less organized radial flows in between. All the flows are cyclonic, at least within a radius of 200 km from the center (cf. Figs. 15a,b). Obviously, this vertical radial-flow profile tends to transport more high-θ_e air in the PBL into the eyewall. It also has the effect of minimizing the erosion of midlevel low-θ_e air (cf. Figs. 15b and 13a) and facilitating the vertical ventilation of mass and moisture, thereby leading to the rapid deepening of the hurricane. Of interest is that air parcels close to the surface accelerate inward until the RMW, where a maximum inflow of greater than 40 m s^{-1} at an elevation of about 500 m is reached, and then they decelerate rapidly to a null speed in the eye. Apparently, this rapid deceleration results from the stiffness of the rotational flow at the RMW where some kind (e.g., gradient wind) of dynamical balance is attained (Ooyama 1982), since the stiffness tends to provide resistance to lateral displacement of the parcels. In contrast, the upper-level radial outflow increases as the stiffness decreases (cf. Figs. 15a,b). Note that a shallow layer of outflow, similar to that found by Hawkins and Imbembo (1976), develops immediately above the inflow layer. Its importance in the development of Andrew will be discussed in a forthcoming article.

The rapid deceleration of radial winds at the RMW is consistent with the development of strong updrafts in the eyewall, as shown in Fig. 15c. The maximum updraft is about 6–8 m s^{-1}, a magnitude similar to that observed in other intense hurricanes (e.g., Jorgensen et al. 1985; Marks and Houze 1987). It is of importance to note that the updrafts in the eyewall, also sloping outward with height, exhibit a multicell structure in the vertical. An examination of the hourly model output shows that these cells tend to preferably develop in three layers: one immediately above the lower-level RMW, one near 700, and the other above 400 hPa. They appear to be more closely related to the surface frictional convergence (cf. Figs. 15b,c), rapid latent heat release (cf. Figs. 11a and 15c) and a secondary heating maximum in the upper-level stratiform region (cf. Figs. 11b and 15b,c). Such a multicell structure has been observed by Marks and Houze (1987) and simulated by Lord et al. (1984) who attributed this feature to the incorporation of ice microphysics. Outside the eyewall, weak ascent occurs in the upper outflow layers, forming the widespread stratiform region. The multicell updraft structures appear too in the spiral rainbands, but they are not as robust as those in the eyewall. Weak compensating subsidence and evaporatively driven downdrafts are also evident between the updrafts; the most intense downdraft exceeds 3 m s^{-1}. Of particular interest is that the maximum downdraft in the eye does not occur at its center but in a narrow zone close to the inner edge of the sloping eyewall, with a magnitude of 1–1.5 m s^{-1}. This descending flow coincides with the downward dip of θ_e close to the eyewall (cf. Figs. 15c and 13a). Jorgensen (1984b) has also analyzed such a strong downdraft in the eye close to an intense sloping updraft in the eyewall of Hurricane Allen (see his Fig. 14).

The vertical relative vorticity field is closely related to the tangential winds shown in Fig. 15a. That is, intense cyclonic (anticyclonic) vorticity occurs along the RMW inside (outside) the sloping eyewall; both are dominated by the shear vorticity (cf. Figs. 15a,d). The cyclonic vorticity is peaked slightly above the surface, with a value of greater than 7.5×10^{-3} s^{-1}. This magnitude is similar to the one observed by Powell and Houston (1996) for Andrew, and it is about 125 times greater than the local Coriolis parameter. The multicell vorticity structures, like the vertical motion, are also evident in the eyewall. The eye is dominated by weaker cyclonic vorticity with a magnitude on the order of 1–3×10^{-3} s^{-1}, except above 200 hPa where a changeover to anticyclonic flow occurs. It is apparent from Figs. 15a–c that the cyclonic vorticity in the eyewall is generated initially in the lower levels through stretching and then advected upward in the eyewall, whereas in the eye the descending flow always tends to reduce slowly the cyclonic vorticity. Tilting of horizontal vorticity appears to have negative contributions to the vorticity production because of the presence of negative vertical shear in the region. Outside the radius of 150 km from the center, the vorticity field is much weaker and less organized due to the absence of strong convergence.

Horizontal flows, shown in Fig. 16, provide further insight into the 3D motion structures in the vicinity of the storm. Note first that the strongest winds at each level coincide with the maximum radar reflectivity and that the RMW increases in radius with height, in agreement with previous observations (e.g., Marks et al. 1992). The low-level flow structure, which is similar to that at the surface (cf. Figs. 16d and 7b), exhibits spiral convergent streams toward the eyewall. At 850 hPa, however, the streamlines in the eye rotate outward while the streamlines from the far distance rotate inward; both converge cyclonically at the eyewall where the maximum convergence is realized. Of course, these air streams are all cross-isobaric under the influence of surface friction, albeit to different degrees. The outward rotation in the eye is consistent with the radial outflow immediately above the lower-level RMW (cf. Figs. 16c and 15b), a feature that has been noted by Marks et al. (1992) and Jorgensen (1984b) from airborne Doppler radar measurements. According to Willoughby (1979), this structure represents a response of the flow to condensational heating in the eyewall and is characteristic of the horizontal divergence and subsidence in the region of the eye (Anthes 1982). The structure is discernible up to a level of 400 hPa. Higher up, the mechanism changes (cf. Figs. 16b and 15c) because the streamlines begin to diverge outward with weak ascent near the eyewall. The divergent outflows do not become dominant until 300 hPa (see Fig. 15b). At 200 hPa, the divergent outflow rotates cyclonically first from the eye and then becomes anticyclonic at a radius of about 200 km as a result of conservation of angular momentum (Fig. 16a). With this flow pattern, snow particles detrained out of the eyewall are advected radially outward and azimuthally around the storm while falling slowly into downdrafts such that the spiral rainbands tend to be homogenized in the upper troposphere, as mentioned earlier (cf. Figs. 16d and 9). In fact, Marks and Houze (1987) have shown that ice particles detrained from the eyewall are carried about one-and-a-half times around the storm by the strong tangential flow before reaching the melting level.

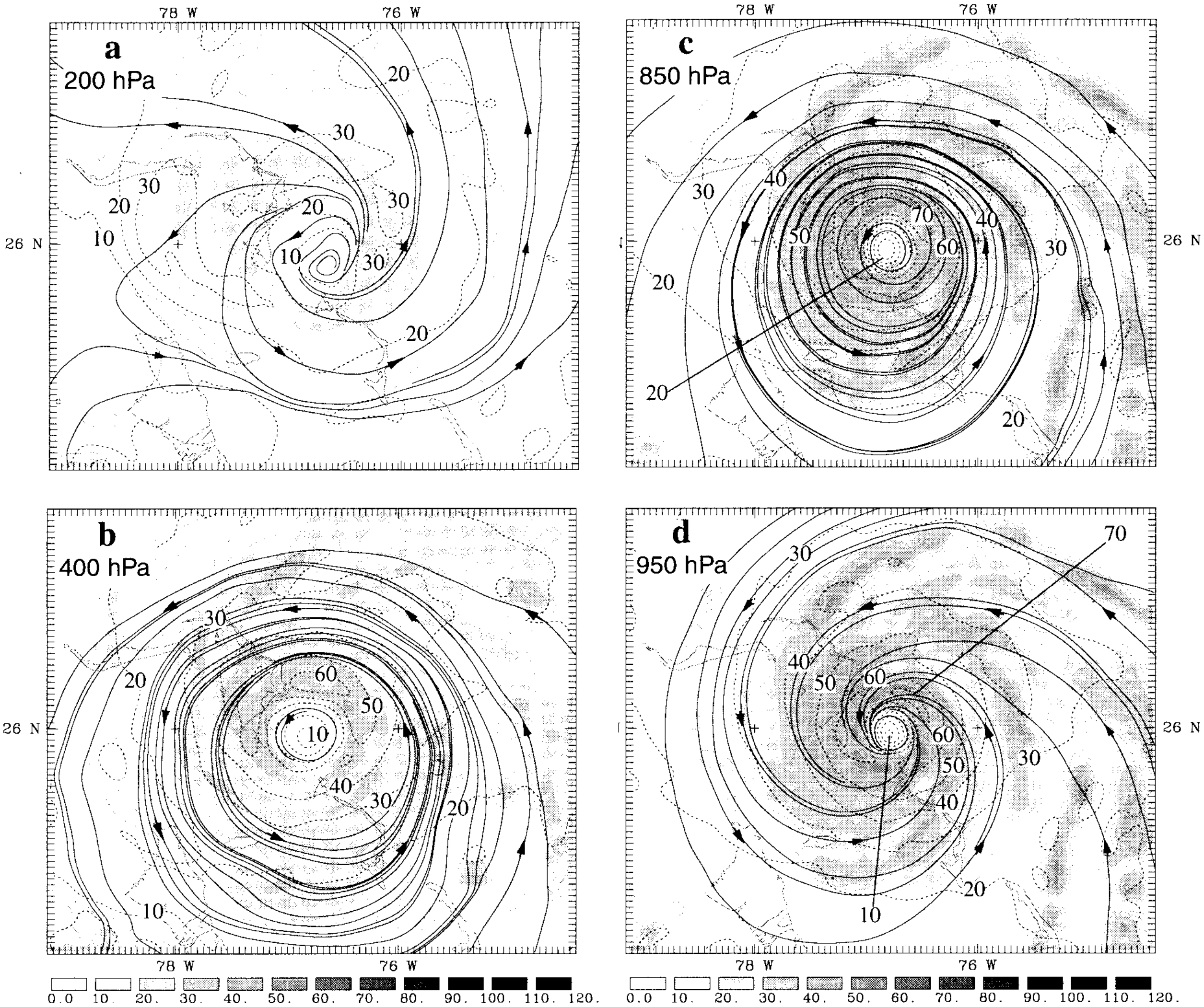

FIG. 16. As in Fig. 9 but for the streamlines (solid) and isotachs (dashed, every 10 m s^{-1}) at (a) 200 hPa, (b) 400 hPa, (c) 850 hPa, and (d) 950 hPa. The simulated reflectivity is superposed with gray scales.

6. Summary and conclusions

In this study, an improved version of the PSU–NCAR nonhydrostatic, movable, triply nested grid model (MM5) is used to provide a multiscale numerical study of Hurricane Andrew (1992), with the finest grid size of 6 km to resolve the inner core of the storm. The model is initialized with the NCEP analysis with modified moisture content over the data-void ocean and incorporation of a model-generated vortex at the model initial time. It is then integrated for 72 h, which covers the most interesting period of Andrew's life cycle, namely, from the time of its developing from a tropical storm to a near–category 5 hurricane near the Bahamas and to its landfall over Florida. The model demonstrates considerable skill in reproducing the multiscale structures and evolution of Hurricane Andrew, as verified against measurements from various observational platform, including satellite, radar, surface, and reconnaissance aircraft as well as observational analyses from earlier studies of hurricanes. The results from our simulation are more realistic than any previously obtained. The most important results are summarized below.

- The model captures successfully the track, propagation, and rapid deepening of the storm during the 3-day period, as verified against the best track analysis. The model reproduces the minimum central pressure of 919 hPa, the rapid deepening rate of greater than 1.5 hPa h^{-1}, and the RMW with a peak surface wind of 66 m s^{-1} along the coast.
- The model simulates well the larger-scale environment in which Andrew is embedded. In particular, the basic characteristics of 49 ODW thermodynamic soundings in the vicinity of the storm are reasonably represented by the simulation. Both the observed and the simulated soundings show the development of a well-mixed boundary layer, the moist lower tropo-

sphere with dry air above in all quadrants. The air-sea interaction process appears to be responsible for the rapid increase of θ_e as air parcels in the PBL move inward from the outer high pressure region while the cloud–radiative interaction process accounts for the generation of intense θ_e gradients in the stratocumulus cloud layer, thereby creating an environment conducive to intense convective overturning along the spiral rainbands and in the eyewall.

- The model reproduces the visible cloud structures in terms of their size, shape, and intensity, as compared to the satellite and radar imagery. The model-simulated hydrometeor is in qualitative agreement with in-situ measurements. In addition, the simulated radar reflectivity calculated from the various prognostic variables for water substances exhibits many structures similar to the observed. They include the eye, the steady and organized deep convection in the eyewall, the cellular convection along the spiral rainbands, the shallow convection at the outer edge, the extensive anvil clouds in the upper outflow layers, and the sharp gradient of reflectivity across the melting level.
- Of particular significance is that *the model produces realistically the inner-core structures of Hurricane Andrew despite the use of the NCEP analysis as the model initial conditions. They include the generation of an echo-free eye that expands in diameter with height, a sloping eyewall with multiple intense updrafts, and precipitation zones in the vertical as well as various types of spiral rainbands.* In agreement with previous observations, the eyewall coincides with the RMW, which accounts for the generation of intense cyclonic vorticity inside and anticyclonic vorticity outside the eyewall. It is shown that the tangential and radial flows, relative vorticity, updrafts, and radar reflectivity are all peaked near the top of the boundary layer, at an elevation of 500–1000 m.
- It is found that *Hurricane Andrew is characterized by a shallow layer of intense cyclonic inflows in the PBL and intense outflows above 300 hPa, with much weaker and less organized radial flows in between.* This inflow profile, coupled with the vertical θ_e structure, facilitates the transport of the boundary layer high-θ_e air, the latent heat release in the eyewall, and thus the explosive deepening of the storm. The inflow accelerates cyclonically and reaches a maximum value of 40 m s^{-1} at the RMW where it decelerates rapidly to a null speed near the core, causing the development of intense convergence and updrafts in the eyewall. On the average, *the central core is dominated by weak (subsiding) horizontally divergent outflows, but with a narrow zone of strong descent occurring at the inner edge of the eyewall.* It is also found that *the streamlines in the central core tend to rotate cyclonically outward and converge in the eyewall with the cyclonic inflows from the far distance.*
- Hurricane Andrew displays an intense warm-core but dry column at the center with a peak warm anomaly of 16°C near 500 hPa and penetrative high-θ_e columns ($>$365 K) close to the eyewall with a blob of minimum θ_e in the midlevel core region. The maximum surface θ_e of 382 K yields a minimum central pressure of 920 hPa, as estimated from the Malkus–Riehl equation, which is close to the simulated value of 919 hPa. The sounding in the eye exhibits a moist boundary layer and a deep layer of dry air above, whereas the eyewall features a deep saturated troposphere with sub-moist-adiabatic lapse rates below the melting level and in the upper outflow layers.

A series of diagnostic analyses of the model output are underway to provide an understanding of the kinematics and dynamics in the core regions and of the multiscale interactions involved in the development of Hurricane Andrew. In addition, a number of sensitivity experiments have been conducted to examine the relative importance of the various parameters in affecting the inner-core structures and evolution of the storm. The results will be reported in future journal publications.

Recognizing that there are some deficiencies with the model simulation due to the use of the imperfect initial conditions and the 6-km grid length that is still too coarse to resolve some convective cells, the above results imply that the interaction of the internal dynamics and thermodynamics of hurricanes with their environments may determine the predictability of the general inner-core structures and evolution of hurricanes, given the SST distribution and tropical synoptic settings. It follows that it may be possible to predict reasonably the track, intensity and inner-core structures of hurricanes from the tropical synoptic conditions when high grid resolution, realistic model physics, and proper initial vortices (size and intensity) in relation to their larger-scale environments are incorporated. Of course, more numerical case studies of hurricanes are needed in order to generalize the above conclusion; the present study only represents the first attempt along this line.

Acknowledgments. We thank James Franklin at the Hurricane Research Division/AOML/NOAA for providing the Omega dropwindsonde data associated with Hurricane Andrew for our model verification. Morris Bender, Russ Elsberry, Bob Houze, and Frank Marks made many constructive comments on an earlier version of the manuscript. This work was supported by the Natural Science and Engineering Research Council of Canada and the U.S. Office of Naval Research. The computations were performed at the National Center for Atmospheric Research, which is sponsored by the National Science Foundation.

REFERENCES

Anthes, R. A., 1972: The development of asymmetries in a three-dimensional numerical model of tropical cyclone. *Mon. Wea. Rev.,* **100,** 461–476.

——, 1982: *Tropical Cyclones—Their Evolution, Structure and Effects.* Amer. Meteor. Soc., 208 pp.

——, E.-Y. Hsie, and Y.-H. Kuo, 1987: Description of the Penn State/NCAR mesoscale model version 4 (MM4). NCAR Tech. Note NCAR/TN-282, 66 pp. [Available from NCAR Publications Office, P. O. Box 3000, Boulder, CO 80307-3000.]

Bender, M. A., R. Ross, R. E. Tuleya, and Y. Kurihara, 1993: Improvements in tropical cyclone track and intensity forecast using the GFDL initialization system. *Mon. Wea. Rev.,* **121,** 2046–2061.

Betts, A. K., and M. J. Miller, 1986: A new convective adjustment scheme. Part II: Single column tests using GATE wave, BOMEX, ATEX and Arctic air-mass data sets. *Quart. J. Roy. Meteor. Soc.,* **112,** 693–709.

Black, R. A., and J. Hallett, 1986: Observations of the distribution of ice in hurricanes. *J. Atmos. Sci.,* **43,** 802–822.

Blackadar, A. K., 1979: High resolution models of the planetary boundary layer. *Advances in Environmental Science and Engineering,* J. Pfafflin and E. Ziegler, Eds., Vol. 1, Gordon and Breach Science Publishers, 50–85.

Burpee, R. W., and M. L. Black, 1989: Temporal and spatial variation of rainfall near the centers of two tropical cyclones. *Mon. Wea. Rev.,* **117,** 2208–2218.

DeMaria, M., and J. D. Pickle, 1988: A simplified system of equations for simulation of tropical cyclones. *J. Atmos. Sci.,* **45,** 1542–1554.

Dudhia, J., 1993: A nonhydrostatic version of the Penn State–NCAR mesoscale model: Validation tests and simulation of an Atlantic cyclone and cold front. *Mon. Wea. Rev.,* **121,** 1493–1513.

Elsberry, R. L., 1979: Applications of tropical cyclone models. *Bull. Amer. Meteor. Soc.,* **60,** 750–762.

Emanuel, K. A., 1986: An air-sea interaction theory for tropical cyclones. Part I: Steady-state maintenance. *J. Atmos. Sci.,* **43,** 585–604.

——, 1988: The maximum intensity of hurricanes. *J. Atmos. Sci.,* **45,** 1143–1155.

Frank, W. M., 1977: The structure and energetics of the tropical cyclone. Part I: Storm structure. *Mon. Wea. Rev.,* **105,** 1119–1135.

Franklin, J. L., S. J. Lord, and F. D. Marks Jr., 1988: Dropwinsonde and radar observations of the eye of Hurricane Gloria. *Mon. Wea. Rev.,* **116,** 1237–1244.

——, ——, S. E. Feuer, and F. D. Marks Jr., 1993: The kinematic structure of Hurricane Gloria (1985) determined from nested analyses of dropwindsonde and Doppler radar data. *Mon. Wea. Rev.,* **121,** 2433–2450.

Fujiyoshi, Y., T. Endoh, T. Yamada, K. Tsuboki, Y. Tachibana, and G. Wakahana, 1990: Determination of a *Z–R* relationship for snowfall using a radar and high sensitivity snow gauges. *J. Appl. Meteor.,* **29,** 147–152.

Gamache, J. F., R. A. Houze, and F. D. Marks, 1993: Dual-aircraft investigation of the inner core of Hurricane Norbert Part III: Water budget. *J. Atmos. Sci.,* **50,** 3221–3243.

Gray, W. M., 1979: Hurricanes: Their formation, structure, and likely role in the tropical circulation. *Meteorology over the Tropical Oceans,* D. B. Shaw, Ed., Roy. Meteor. Soc., 155–199.

——, and D. J. Shea, 1973: The hurricanes inner core region II. Thermal stability and dynamic characteristics. *J. Atmos. Sci.,* **30,** 1565–1576.

Grell, G. A., J. Dudhia, and D. R. Stauffer, 1995: A description of the fifth generation Penn State/NCAR mesoscale model (MM5). NCAR Tech Note NCAR/TN-398+STR, 138 pp. [Available from NCAR Publications Office, P. O. Box 3000, Boulder, CO 80307-3000.]

Hawkins, H. F., and S. M. Imbembo, 1976: The structure of a small, intense hurricane, Inez 1966. *Mon. Wea. Rev.,* **104,** 418–442.

Holland, G. J., and R. T. Merrill, 1984: On the dynamics of tropical cyclone structure changes. *Quart. J. Roy. Meteor. Soc.,* **110,** 723–745.

Holliday, C. R., and A. H. Thompson, 1979: Climatological characteristics of rapidly intensifing typhoons. *Mon. Wea. Rev.,* **107,** 1022–1034.

Houze, R. A., Jr., F. D. Marks Jr., and R. A. Black, 1992: Dual-aircraft investigation of the inner core of the Hurricane Norbert. Part II: Mesoscale distribution of ice particles. *J. Atmos. Sci.,* **49,** 943–962.

Jones, R. W., 1977: A nested grid for a three-dimensional model of tropical cyclone. *J. Atmos. Sci.,* **34,** 1528–1533.

Jorgensen, D. P., 1984a: Mesoscale and convective scale characteristics of nature hurricanes. Part I: General observations by aircraft. *J. Atmos. Sci.,* **41,** 1268–1285.

——, 1984b: Mesoscale and convective scale characteristics of nature hurricanes. Part II: Inner core structure of Hurricane Allen (1980). *J. Atmos. Sci.,* **41,** 1287–1311.

——, and P. T. Willis, 1982: A *Z–R* relationship for hurricanes. *J. Appl. Meteor.,* **21,** 356–366.

——, E. J. Zipser, and M. A. LeMone, 1985: Vertical motions in intense hurricanes. *J. Atmos. Sci.,* **42,** 839–856.

Kain, J. S., and J. M. Fritsch, 1992: Convective parameterization for mesoscale models: The Kain–Fritsch scheme. *The Representation of Cumulus Convection in Numerical Models, Meteor. Monogr.,* No. 46, Amer. Meteor. Soc., 165–170.

Kasahara, A., 1961: A numerical experiment on the development of tropical cyclone. *J. Meteor.,* **18,** 259–282.

Klemp, J. B., and R. B. Wilhelmson, 1978: Simulations of three-dimensional convective storm dynamics. *J. Atmos. Sci.,* **35,** 1070–1069.

Krishnamurti, T. N., D. Oosterhof, and N. Dignon, 1989: Hurricane prediction with a high-resolution global model. *Mon. Wea. Rev.,* **117,** 631–669.

——, K. S. Yap, and D. K. Oosterhof, 1991: Sensitivity of tropical storm forecast to radiative destabilization. *Mon. Wea. Rev.,* **119,** 2176–2204.

——, S. K. Bhowmik, D. Oosterhof, and G. Rohaly, 1995: Mesoscale signatures within the Tropics generated by physical initialization, *Mon. Wea. Rev.,* **123,** 2771–2790.

Kuo, H.-L., 1965: On formation and intensification of tropical cyclones through latent heat release by cumulus convection. *J. Atmos. Sci.,* **22,** 40–63.

——, 1974: Further studies of the parameterization of the influence of cumulus convection on large-scale flow. *J. Atmos. Sci.,* **31,** 1232–1240.

Kurihara, Y., 1973: A scheme of moist convective adjustment. *Mon. Wea. Rev.,* **101,** 547–553.

——, 1985: Numerical modeling of tropical cyclones. *Advances in Geophysics,* Vol. 28B, Academic Press, 255–280.

——, and M. A. Bender, 1982: Structure and analysis of the eye of a numerically simulated tropical cyclone. *J. Meteor. Soc. Japan,* **60,** 381–395.

——, ——, and R. Ross, 1993: An initialization scheme of hurricane models by vortex specification. *Mon. Wea. Rev.,* **121,** 2030–2045.

——, ——, R. E. Tuleya, and R. Ross, 1995: Improvements in the GFDL hurricane prediction system. *Mon. Wea. Rev.,* **123,** 2791–2801.

Lin, Y. L., R. D. Farley, and H. D. Orville, 1983: Bulk parameterization of the snow field in a cloud model. *J. Climate Appl. Meteor.,* **22,** 1065–1092.

Lord, S. J., H. E. Willoughby, and J. M. Piotrowicz, 1984: Role of a parameterized ice-phase microphysics in an axisymmetric, nonhydrostatic tropical cyclone model. *J. Atmos. Sci.,* **41,** 2836–2848.

Malkus, J. S., and H. Riehl, 1960: On the dynamics and energy transformations in steady-state hurricanes. *Tellus,* **12,** 1–20.

Marks, F. D., Jr., 1985: Evolution and structure of precipitation in Hurricane Allen (1980). *Mon. Wea. Rev.,* **113,** 909–930.

——, and R. A. Houze Jr., 1987: Inner core structure of Hurricane Alicia from airborne Doppler-radar observations. *J. Atmos. Sci.,* **44,** 1296–1317.

——, ——, and J. F. Gamache, 1992: Dual-aircraft investigation of the inner core of the Hurricane Norbert. Part I: Kinematic structure. *J. Atmos. Sci.,* **49,** 919–942.

Mayfield, M., L. Avila, and E. N. Rappaport, 1994: Annual summaries: Atlantic hurricane season of 1992. *Mon. Wea. Rev.,* **122,** 517–538.

Molinari, J., and M. Dudeck, 1992: Parameterization of convective precipitation in mesoscale numerical models: A critical review. *Mon. Wea. Rev.,* **120,** 326–344.

——, and D. Vollaro, 1995: External influences on hurricane intensity. Part II: Vertical structure and response of the hurricane vortex. *J. Atmos. Sci.,* **52,** 3593–3606.

NOAA, 1992: *Storm Data.* Department of Commerse Rep. 34 (8). [Available from National Climate Data Center, 37 Battery Park Ave., Asheville, NC 28801-2733.]

Ooyama, K., 1969: Numerical simulation of the life-cycle of tropical cyclones. *J. Atmos. Sci.,* **26,** 3–40.

——, 1982: Conceptual evolution of the theory and modeling of the tropical cyclone. *J. Meteor. Soc. Japan,* **60,** 369–380.

Parrish, J. R., R. W. Burpee, F. D. Marks Jr., and R. Grebe, 1982: Rainfall patterns observed by digitized radar during landfall of Hurricane Frederic (1979). *Mon. Wea. Rev.,* **110,** 1933–1944.

Perkey, D. J., and W. Kreitzberg, 1976: A time-dependent lateral boundary scheme for limited area primitive equation models. *Mon. Wea. Rev.,* **104,** 744–755.

Powell, M. D., and S. H. Houston, 1996: Hurricane Andrew's landfall in Florida. Part II: surface wind fields and potential real-time application. *Wea. Forecasting,* **11,** 329–349.

Rappaport, E. N., 1994: Hurricane Andrew. *Weather,* **49,** 51–61.

Rosenthal, S. L., 1978: Numerical simulation of tropical cyclone development with latent heat release by resolvable scales. I: Model description and preliminary results. *J. Atmos. Sci.,* **35,** 258–271.

Ross, R. J., and Y. Kurihara, 1995: A numerical study on influences of Hurricane Gloria (1985) on the environment. *Mon. Wea. Rev.,* **123,** 332–346.

Rotunno, R., and K. A. Emanuel, 1987: An air-sea interaction theory for tropical cyclones. Part II: Evolutionary study using a nonhydrostatic axisymmetric numerical model. *J. Atmos. Sci.,* **44,** 542–561.

Roux, F., and N. Viltard, 1995: Structure and evolution of Hurricane Claudettte on 7 September 1991 from airborne Doppler radar observation. Part I: Kinematics. *Mon. Wea. Rev.,* **123,** 2611–2639.

Shapiro, L. J., and H. E. Willoughby, 1982: The response of the balanced hurricanes to local sources of heat and momentum. *J. Atmos. Sci.,* **39,** 378–394.

Simpson, R. H., 1974: The hurricane disaster-potential scale. *Weatherwise,* **27,** 169.

Smith, P. L., 1984: Equivalent radar reflectivity factors for snow and ice particles. *J. Climate Appl. Meteor.,* **23,** 1258–1260.

Smolarkiewicz, P., and G. A. Grell, 1992: A class of monotone interpolation schemes. *J. Comput. Phys.,* **101,** 431–440.

Sunqvist, H., 1970: Numerical simulation of the development of tropical cyclones with ten-level model. Part I. *Tellus,* **22,** 359–390.

Tao, W.-K., and J. Simpson, 1993: The Goddard cumulus ensemble model. Part I: Model description. *Terr. Atmos. Oceanic Sci.,* **4,** 35–72.

Tripoli, G. J., 1992: An explicit three-dimensional nonhydrostatic numerical simulation of a tropical cyclone. *Meteor. Atmos. Phys.,* **49,** 229–254.

Tuleya, R. E., M. A. Bender, and Y. Kurihara, 1984: A simulation study of the landfall of tropical cyclones using a movable nested-mesh model. *Mon. Wea. Rev.,* **112,** 124–136.

Wakimoto, R. M., and P. G. Black, 1994: Damage survey of Hurricane Andrew and its relationship to the eyewall. *Bull. Amer. Meteor. Soc.,* **75,** 189–200.

Willoughby, H. E., 1979: Forced secondary circulations in hurricanes. *J. Geophys. Res.,* **84,** 3173–3183.

——, 1990: Temporal changes of the primary circulation in tropical cyclones. *J. Atmos. Sci.,* **47,** 242–264.

——, and P. G. Black, 1996: Hurricane Andrew in Florida: Dynamics of a disaster. *Bull. Amer. Meteor. Soc.,* **77,** 543–549.

——, J. A. Clos, and M. G. Shoreibah, 1982: Concentric eyewalls, secondary wind maxima, and the evolution of the hurricane vortex. *J. Atmos. Sci.,* **39,** 395–411.

——, H. L. Jin, S. J. Lord, and J. M. Piotrowicz, 1984a: Hurricane structure and evolution as simulated by an axisymmetric, nonhydrostatic numerical model. *J. Atmos. Sci.,* **41,** 1169–1186.

——, F. D. Marks Jr., and R. J. Feinberg, 1984b: Stationary and moving convective bands in hurricanes. *J. Atmos. Sci.,* **41,** 3189–3211.

Yamasaki, M., 1977: A preliminary experiment of the tropical cyclone without parameterizing the effects of cumulus convection. *J. Meteor. Soc. Japan,* **55,** 11–30.

Zhang, D.-L., 1989: The effect of parameterized ice microphysics on the simulation of vortex circulation with a mesoscale hydrostatic model. *Tellus,* **41A,** 132–147.

——, and R. A. Anthes, 1982: A high-resolution model of the planetary boundary layer—Sensitivity tests and comparisons with SESAME-79 data. *J. Appl. Meteor.,* **21,** 1594–1609.

——, E.-Y. Hsie, and M. W. Moncrieff, 1988: A comparison of explicit and implicit predictions of convective and stratiform precipitating weather systems with a meso-β scale numerical model. *Quart. J. Roy. Meteor. Soc.,* **114,** 31–60.